

SEARCHING FOR LONG-LIVED DARK PHOTONS WITH THE HEAVY PHOTON SEARCH EXPERIMENT

A DISSERTATION
SUBMITTED TO THE DEPARTMENT OF PHYSICS
AND THE COMMITTEE ON GRADUATE STUDIES
OF STANFORD UNIVERSITY
IN PARTIAL FULFILLMENT OF THE REQUIREMENTS
FOR THE DEGREE OF
DOCTOR OF PHILOSOPHY

Matthew Reagan Solt

June 2020

¹²

© Copyright by Matthew Reagan Solt 2020
All Rights Reserved

¹³

I certify that I have read this dissertation and that, in my opinion, it is fully adequate in scope and quality as a dissertation for the degree of Doctor of Philosophy.

¹⁴

(Philip Schuster) Principal Adviser

I certify that I have read this dissertation and that, in my opinion, it is fully adequate in scope and quality as a dissertation for the degree of Doctor of Philosophy.

¹⁵

(John Jaros)

I certify that I have read this dissertation and that, in my opinion, it is fully adequate in scope and quality as a dissertation for the degree of Doctor of Philosophy.

¹⁶

(Dan Ackerib)

I certify that I have read this dissertation and that, in my opinion, it is fully adequate in scope and quality as a dissertation for the degree of Doctor of Philosophy.

¹⁷

(Pat Burchat)

Approved for the Stanford University Committee on Graduate Studies

¹⁸

¹⁹ **Abstract**

²⁰ A heavy photon (also called a dark photon or A') is a hypothetical vector boson that arises from a
²¹ massive $U(1)$ abelian gauge symmetry. Because of the ability of heavy photons to kinetically mix
²² with the Standard Model photon, they are connected to many of hidden sector models and are
²³ favored for a variety of dark sector scenarios, particularly for dark matter at the sub-GeV mass scale.
²⁴ The Heavy Photon Search Experiment (HPS) is a fixed target experiment at Jefferson Laboratory
²⁵ dedicated to searching for heavy photons in the MeV - GeV mass range and kinetic mixing strength
²⁶ $\epsilon^2 \sim 10^{-5} - 10^{-10}$. It does so through two distinct searches - a search for a narrow mass resonance
²⁷ and, for sufficiently small couplings, a search for secondary vertices beyond a large prompt QED
²⁸ background.

²⁹ In order to perform such searches, the HPS apparatus is a compact forward acceptance spectrometer
³⁰ that must be able to reconstruct particle masses and vertices with extreme precision. Heavy
³¹ photons are electro-produced from a continuous electron beam incident on a thin tungsten foil, and
³² HPS is able to reconstruct momentum of the subsequent decays to e^+e^- pairs through a silicon
³³ vertex tracker (SVT). HPS currently has three datasets - an Engineering Run in 2015 and 2016
³⁴ as well as a physics run with an upgraded detector in 2019 - all at different energies and beam
³⁵ currents. Presented in this dissertation are heavy photon physics and motivations, introduction to
³⁶ the HPS detector and reconstruction, upgrades and other models of interest, and the results from
³⁷ displaced vertex search from the HPS 2016 Engineering Run which was taken with a 2.3 GeV, 200
³⁸ nA continuous electron beam and collected a total of luminosity nb^{-1} (equivalent to days days of
³⁹ continuous uptime).

⁴⁰ This dissertation presents results...



Figure 1: This is my current placeholder figure.

⁴¹ Acknowledgments

⁴² I would like to thank a very long list of people...

Contents

43	Abstract	iv
45	Acknowledgments	vi
46	1 The HPS Detector	2
47	1.1 The Continuous Electron Beam Accelerator Facility (CEBAF)	3
48	1.2 Hall B and HPS Beamline	5
49	1.3 Silicon Vertex Tracker	10
50	1.3.1 Sensors and Readout	12
51	1.3.2 SVT Mechanicals	15
52	1.3.3 SVT Data Acquisition, Power, and Services	18
53	1.4 Electromagnetic Calorimeter and Trigger	21
54	1.5 Datasets	25
55	2 Event Reconstruction & Selection	26
56	2.1 HPS Coordinate Systems	26
57	2.2 Ecal Reconstruction	28
58	2.3 SVT Reconstruction	29
59	2.3.1 SVT Hit Reconstruction	29
60	2.3.2 SVT Cluster and 3D Hit Reconstruction	30
61	2.3.3 Track Reconstruction	31
62	2.4 Track Cluster Matching	33
63	2.5 Vertexing	34
64	2.6 Hit Efficiency	37
65	2.7 Tracker Alignment	39
66	2.8 Track-Truth Matching	41
67	2.9 Monte Carlo Samples	43
68	2.10 e^+e^- Preselection Cuts	47
69	2.11 Run Quality, Event Quality, & Data Normalization	48

₇₁ List of Tables

₇₂ 1.1	A summary of the basic parameters for different layers in the SVT.	11
₇₃ 1.2	Summary of the pairs1 Trigger Selection from the 2016 Engineering Run.	24
₇₄ 2.1	Basis for several different coordinate systems used in the HPS reconstruction and analysis.	26
₇₅ 2.2	Requirements applied to V_0 particles during the reconstruction stage for data (i.e. MOUSE cuts).	34
₇₆ 2.3	Requirements applied to V_0 particles during the reconstruction stage for MC (i.e. MOUSE cuts).	34
₇₇ 2.4	Event generators and statistics for MC samples.	43
₇₈ 2.5	Basic generator level physics requirements for different physics processes.	45
₇₉ 2.6	Requirements applied to V_0 after reconstruction as an initial set to study. The time offset for data is 56 ns and the time offset for MC is 43 ns.	47
₈₀ 2.7	Normalization parameters for the RAD, Tritrig, and WAB samples	48

⁸⁵ List of Figures

⁸⁶ 1	This is my current placeholder figure.	v
⁸⁷ 1.1	A 3D rendering of the HPS detector complete with the silicon vertex tracker (SVT), ⁸⁸ electromagnetic calorimeter (Ecal), and chicane.	2
⁸⁹ 1.2	The rate of electrons in at the first layer of the SVT from the so-called “wall of flame” ⁹⁰ - beam electrons that lose energy due to bremmstrahlung in the target and bend in ⁹¹ the magnetic field. To avoid the radiation damage from the wall of flame, the detector ⁹² is split into top and bottom halves.	3
⁹³ 1.3	A schematic of the upgraded Continuous Electron Beam Accelerator Facility (CE- ⁹⁴ BAF) at Jefferson Laboratory. The machine is a recirculating linear accelerator de- ⁹⁵ signed to send a beam of electrons of different currents and energies to four different ⁹⁶ experimental halls (Halls A - D).	4
⁹⁷ 1.4	A schematic of Hall B including the CLAS-12 spectrometer and the HPS detector in ⁹⁸ the Hall B alcove. The electron beam enters the hall from the left in this picture. . .	5
⁹⁹ 1.5	An example of a scan from the 2H02 wire harp from the 2016 Engineering Run. This ¹⁰⁰ provides a measurement of the beam profile that is useful as in input to tuning the ¹⁰¹ beam to its optimal profile at the target. The profile shows a width of 92 μm in x ¹⁰² and 14 μm in y with minimal beam tails.	7
¹⁰³ 1.6	A schematic of the HPS beamline inside the Hall B alcove.	8
¹⁰⁴ 1.7	An example of an SVT wire scan measurement from the 2016 Engineering Run. This ¹⁰⁵ provides a measurement of the beam profile as close to the target as possible. This ¹⁰⁶ scan shows a beam with a 14 μm width in the y -direction with minimal tails and 35 ¹⁰⁷ μm from the nominal beam plane. This is an excellent beam profile for HPS.	9
¹⁰⁸ 1.8	A measurement of the beam halo from 2015 Engineering Run using the occupancy of ¹⁰⁹ the first layer of the SVT in a no target run. The beam halo shows a width of 960 μm ¹¹⁰ and 5 orders of magnitude less than the peak of the beam.	9

111	1.9 A schematic of the HPS silicon vertex tracker (SVT) which includes 6 layers of silicon 112 microstrip sensors inside a vacuum and a uniform magnetic field. Maybe find a better 113 picture.	10
114	1.10 A schematic of the APV25 deep submicron readout chip that was originally designed 115 for CMS detectors but is used for the HPS SVT.	12
116	1.11 A picture of the two SVT sensors (end to end) with each sensor. The sensors are 117 readout by APV25 chips which are housed on a hybrid circuit.	13
118	1.12 The APV25 Shaper schematic. The parameters VFS (related to the input voltage) 119 and isha (related to the input current) were optimized for improved time resolution 120 and reduced pileup.	14
121	1.13 A single SVT module which comprises of two silicon microstrip sensors which are axial 122 (front) and stereo (back) to the beam plane. Each sensor is supported by a carbon 123 fiber support structure can be seen protruding from the right of the axial sensor. . . .	15
124	1.14 Layers 1 - 3 modules of the SVT (from left to right) are place in one of the U-channels. 125 Copper cooling lines and electrical lines can be seen. The wire frames and scan wires 126 can also be seen on the left.	16
127	1.15 A picture inside the SVT vacuum chamber with everything installed except for the 128 target. The frontend boards (FEBs) and FEB cooling plate are on the left. The SVT 129 cooling lines protrude outward in the picture. The first layer of the SVT can be seen 130 in the back behind the wire frames. The SVT is in its closed position and the beam 131 must go through the 1 mm gap between the top and bottom sensors.	17
132	1.16 A schematic of the SVT DAQ system described in Sec. 1.3.3.	18
133	1.17 The FEB cooling plate complete with 10 FEBs fastened to the front and back of the 134 plate.	20
135	1.18 A rendering of the HPS Ecal. Each segment is one of the 442 lead tungstate crystals 136 and the Ecal is split in half to avoid radiation damage from the most intense parts of 137 the beam.	21
138	1.19 A schematic of a PbWO ₄ crystal in the Ecal.	22
139	1.20 A schematic of the trigger for the Ecal. Top and bottom halves of the Ecal are each are 140 readout by FADC readout boards, and then sent to the SSP where a trigger decision 141 is made.	23
142	1.21 A summary for the integrated charge over time for the Top: 2015 Engineering Run 143 and Bottom: 2016 Engineering Run. Replace these figures	25
144	2.1 A schematic of the linear collider tracking parameters 2.1 [12].	27
145	2.2 The run-dependent average position in z for unconstrained vertices fit represented by 146 solid points and a solid line for data and MC simulation, respectively.	35

147	2.3	The run-dependent mean (left) and width (right) in x and y for the unconstrained vertex position in data. The MC is represented as a solid line.	36
148			
149	2.4	Left: The measured SVT layer 1 efficiency for electrons in layer 1 bottom stereo sensor. The MC does not have the correct hit efficiencies. Right: The layer 1 hit efficiency as a function of track slope ($\tan\lambda$) used for the hit killing algorithm described in Sec Section . Replace these figures. Add a positron hit efficiency plot.	37
150			
151			
152			
153	2.5	The target position is found to be -4.3 mm. I actually need to get these plots. Some placeholders are there for now.	39
154			
155	2.6	Preselection and layer 1 requirements for tritrig-wab-beam MC for e^+ and e^- tracks. Left: Purity. Right: Layers with a bad hit. Redo these plots	41
156			
157	2.7	Left pictures show Feynman diagrams for A' (top), RAD (middle) and BH (bottom) events. Right picture shows WAB process.	44
158			
159	2.8	Integrated cross section for the RAD (left), Trident-Trig(middle) and WAB(right) samples, separately.	48
160			

¹⁶¹ This thesis is dedicated to...

¹⁶² **Chapter 1**

¹⁶³ **The HPS Detector**

¹⁶⁴ The Heavy Photon Search (HPS) is a precision vertexing experiment designed to measure both
¹⁶⁵ prompt and long-lived heavy photons that decay to e^+e^- pairs. The HPS detector is a large, compact
¹⁶⁶ forward acceptance spectrometer with three main components - a silicon vertex tracker (SVT), an
¹⁶⁷ electromagnetic calorimeter (Ecal), and a three-magnet chicane. A rendering of the detector is
¹⁶⁸ shown in Fig. 1.1. The SVT used to measure track particles and measure their momentum, the
¹⁶⁹ Ecal is used for timing and triggering, and the analyzing magnet (the middle magnet of the chicane)
¹⁷⁰ bends charged particles for a momentum measurement and particle identification.

¹⁷¹ The specific design of the detector components are optimized for the physics goals of HPS.
¹⁷² To maximize A' 's signal yield, particularly low mass and displaced A' 's, the detector must have
¹⁷³ acceptance to small angles. The search for displaced vertices is limited by vertex resolution that
¹⁷⁴ is dominated by multiple scattering, thus the first layer must be placed as close to the target as
¹⁷⁵ possible.

¹⁷⁶ Beam electrons that are elastically scattered in the target are the dominate source of background
¹⁷⁷ and can be tolerated with a selective trigger. The beam electrons that lose energy in the target due

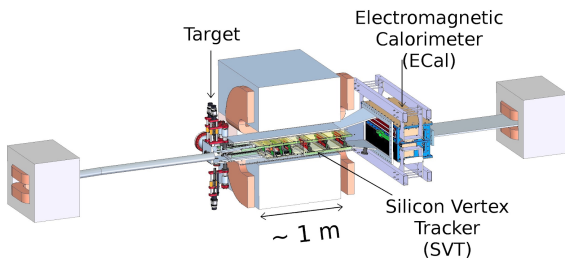


Figure 1.1: A 3D rendering of the HPS detector complete with the silicon vertex tracker (SVT), electromagnetic calorimeter (Ecal), and chicane.

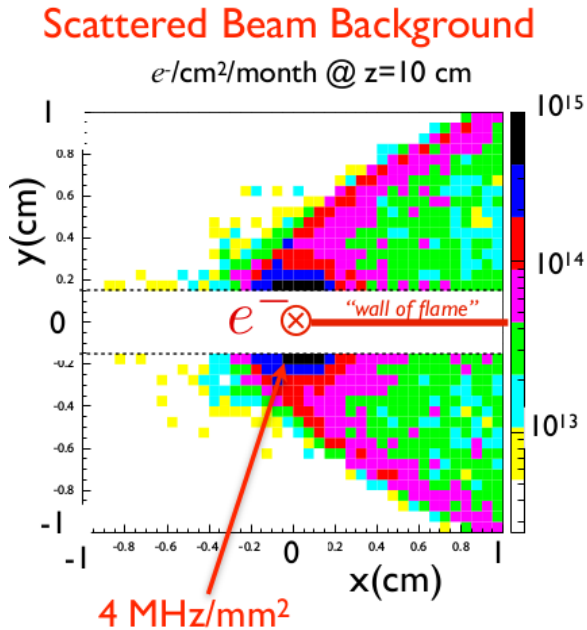


Figure 1.2: The rate of electrons in at the first layer of the SVT from the so-called “wall of flame” - beam electrons that lose energy due to bremmstrahlung in the target and bend in the magnetic field. To avoid the radiation damage from the wall of flame, the detector is split into top and bottom halves.

178 to Bremsstrahlung bend in the presence of the magnetic field and form the so-called “wall of flame”
 179 that would produce too much radiation damage in any detector component as shown in Fig. 1.2.
 180 Thus, the SVT and Ecal are both split in top/bottom halves and placed as close to the beam plane
 181 as possible. In order to balance between maximizing signal yield, optimal vertexing resolution, and
 182 radiation damage, the detector is designed at an opening angle of 15 mrad from the beam plane for
 183 both top and bottom halves.

184 The last major design consideration is due to the fact that there exist a possibility for a beam-gas
 185 interaction downstream of the target that will mock a downstream decay and look very signal-like.
 186 For this reason, the SVT and Ecal are under vacuum. As a result, all materials must be vacuum
 187 compatible (and are tested in a high vacuum test chamber). In addition, all materials must be
 188 nonmagnetic because the SVT operates in a high magnetic field.

189 1.1 The Continuous Electron Beam Accelerator Facility (CE- 190 BAF)

191 The high energy electron beam used for A' production by bremsstrahlung on a thin target is provided
 192 by Jefferson Laboratory’s Continuous Electron Beam Accelerator Facility (CEBAF). CEBAF is able

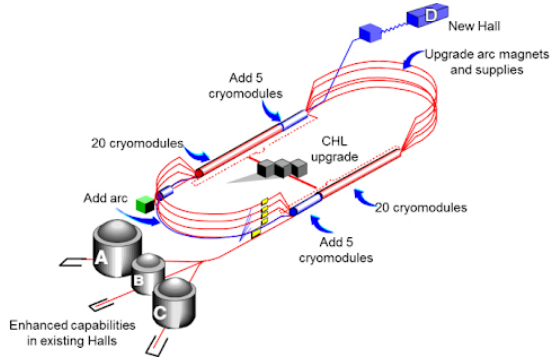


Figure 1.3: A schematic of the upgraded Continuous Electron Beam Accelerator Facility (CEBAF) at Jefferson Laboratory. The machine is a recirculating linear accelerator designed to send a beam of electrons of different currents and energies to four different experimental halls (Halls A - D).

193 to simultaneously deliver intense and energetic electron beams of different energies and currents to
 194 three different experimental halls (Hall A, Hall B, and Hall C). The recent upgrade allows for CEBAF
 195 to deliver beam to four experimental halls (an additional Hall D) in multiples of 2.2 GeV up to 12
 196 GeV. Beyond and including the 2015 Engineering Run, HPS runs have all been in the 12 GeV era -
 197 that is with the upgrades.

198 CEBAF is a recirculating linear accelerator (linac) designed as a “racetrack” configuration where
 199 beam bunches are circulated multiple times through the same two linacs by arcs as shown in Fig.
 200 1.3. Each cycle, or pass, around the accelerator adds an additional 2.2 GeV of beam energy for a
 201 maximum of 5 passes to Hall A, Hall B, and Hall C and an additional half pass to Hall D. Thus,
 202 the energy in a hall will be $0.1 \text{ GeV} + n \times 2.2 \text{ GeV}$ for n passes (the addition 0.1 GeV comes from
 203 the energy from the injector). CEBAF can deliver a beam current of up to $85 \mu\text{A}$ to halls A and C
 204 and deliver up to $5 \mu\text{A}$ to halls B and D (HPS utilizes a current far less than the maximum).

205 Electrons in the accelerator originate from the photoemission of a strained GaAs superlattice
 206 photocathode with an incident laser of 780 nm wavelength, which is equal to the band gap of the
 207 GaAs [13]. The incident laser is pulsed at 499 MHz for ≈ 40 ps. The photoemitted electrons are
 208 then brought to the the injector before finally entering the accelerator.

209 CEBAF accelerates electrons using superconducting radiofrequency (RF) cavities operating at
 210 1500 MHz and by using an RF separator, can deliver beam pulses at either 500 MHz or 250 MHz,
 211 essentially a continuous duty cycle, to each of the four experimental halls. The continuous duty cycle
 212 is essential to HPS as it reduces pileup effects while maximizing luminosity. The 12 GeV upgrade
 213 included a 750 MHz RF separator which allowed the beam to be diverted to the new Hall D.

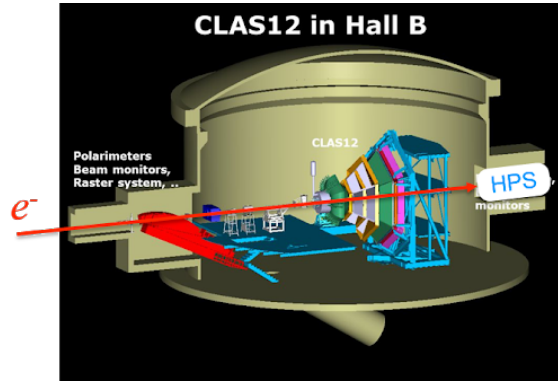


Figure 1.4: A schematic of Hall B including the CLAS-12 spectrometer and the HPS detector in the Hall B alcove. The electron beam enters the hall from the left in this picture.

214 1.2 Hall B and HPS Beamline

215 The HPS experiment is located in Hall B in an alcove behind the CLAS12 (CEBAF Large-Acceptance
216 Spectrometer) detector, which is typically used for low-current precision nuclear physics. Hall B can
217 receive either an electron or photon beam. In order to reduce pileup and beam background for
218 the HPS experiment, the Hall B beam from CEBAF is a continuous beam structure with a bunch
219 spacing at 2 ns (which is far shorter than the trigger window and comparable to the detector timing
220 resolution).

221 The Hall B beamline begins with a large tagger dipole magnet which is a dipole magnet which,
222 when energized, steers the electron beam into the tagger dump below the beamline. The tagger
223 magnet is far upstream of HPS and allows for tuning of the beam to an acceptable quality before
224 delivering the beam to HPS. This is critical as the low acceptance of the tracker puts the silicon
225 within 5 mm of the nominal beam plane even with the SVT fully retracted, thus a poor quality
226 beam (one with a large spotsize, beam tails, or other instabilities) could cause unnecessary radiation
227 damage to the detector. If a target is placed upstream of the tagger magnet, a photon beam can
228 also be produced in Hall B which has been used for test runs for HPS in the past. The nominal
229 configuration for HPS physics running is for the tagger magnet to be de-energized so that the electron
230 beam can be delivered to HPS.

231 The beamline between the tagger magnet and HPS consists of several beam position monitors
232 (BPMs) which measure the passing beam bunches to provide an estimate of beam current and posi-
233 tion. A series of quadrupole magnets and H/V correctors on the beamline are used for fast automatic
234 correction to beam trajectories based on the BPM measurements. The quadrupole magnets are also
235 used to squeeze the beam spotsize as small as possible at the target.

236 The Hall B beamline also includes several wire harps to measure the beam position and profile.
237 This is used for beam tuning as well as to ensure the beam is safe enough to perform wire scans

with the wires directly connected to the SVT as described below. An example of a harp scan from the 2H02 harp, which is the closest wire harp to the HPS target at 2.2 m upstream, from the 2016 Engineering Run is shown in Fig. 1.5. The general strategy to achieve a small spot size at the target is to use the measurements from the 2H02 wire harp as well as several wire harps further upstream in conjunction with a series of quadrupole magnets along the beamline. The magnetic fields of the quadrupole magnets can be finely tune such that the waist, that is the minimum beamspot size in the y -direction, is precisely at the target.

There are several collimators along the beamline to protect both HPS silicon sensors and electronic components from radiation damage from either a stray beam or particles produced by a stray beam. When enough of a beam interacts with a collimator, it also produces a bunch of particles that trip the FSD. The closest collimator to the SVT is a 1 cm thick tungsten plate with machined slots of different widths connected to a linear shift and placed 2.9 m upstream of target (referred to as the “SVT collimator”). With the exception of the inner strips of layer 1 of the SVT, this protects most of the detector from beam tails and beam halo. The collimator can also force an FSD trip such as when the beam is mis-steered or scrapes the collimator which can produce enough secondary particles for the FSD counters to cross threshold. For the 2016 Engineering Run, the 4 mm slot was used ([Is this true??](#)).

Downstream of HPS, there are two fluorescent screens and a screen used for optical transition radiation (OTR) that are useful for viewing the beam position. Finally, the beam is terminated in a Faraday cup in the Hall B beam dump. The Faraday cup provides the most accurate measurement of the total beam charge and is used to normalize the data for the analysis. A beam blocker must be put in front of the Faraday cup at operating beam currents to avoid overheating, and the actual measurement of integrated charge must be re-scaled.

A schematic of the HPS beamline in the Hall B alcove is shown in Fig. 1.6. The HPS apparatus is a large, compact forward spectrometer that consists of a three-magnet chicane system, SVT, Ecal, and a vacuum chamber. On the exterior of HPS, there are several halo counters (plastic scintillators) that monitor the stability of beam conditions. If these halo counters measure particle rates above their set threshold, most likely due to an obscured beam, a fast shut down (FSD) is applied to the Hall B beam within 1 ms to prevent further radiation damage to the HPS detector components.

Thin wires are attached to both the top and bottom of the SVT as described in Sec. 1.3.2 and are used to measure the beam position and profile with respect to the SVT as close to the target as possible. Each half the SVT contains a horizontal and a diagonal wire (oriented $\approx 10^\circ$ from horizontal) for a vertical and horizontal position measurement. These wires move with the SVT and, as they traverse the beam profile, beam particles are scattered into the halo counters on the exterior of HPS. The rate of beam particles counted by the halo counters is proportional to the intensity of the beam, thus through a mapping of the wire position and count rate a beam profile can be produced. In order to ensure safe operation of the SVT, the beam profile in the y -direction

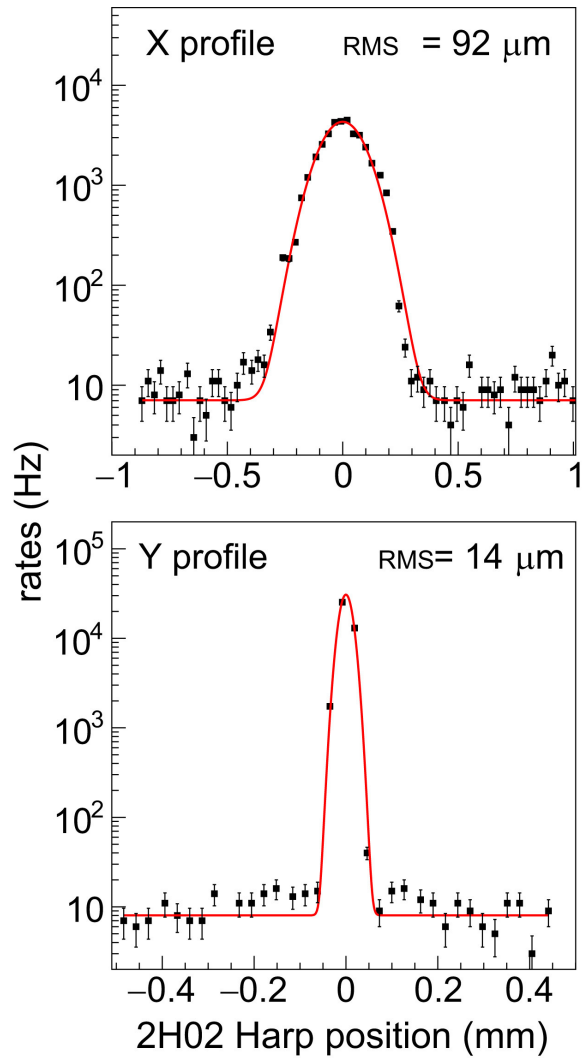


Figure 1.5: An example of a scan from the 2H02 wire harp from the 2016 Engineering Run. This provides a measurement of the beam profile that is useful as input to tuning the beam to its optimal profile at the target. The profile shows a width of $92 \mu\text{m}$ in x and $14 \mu\text{m}$ in y with minimal beam tails.

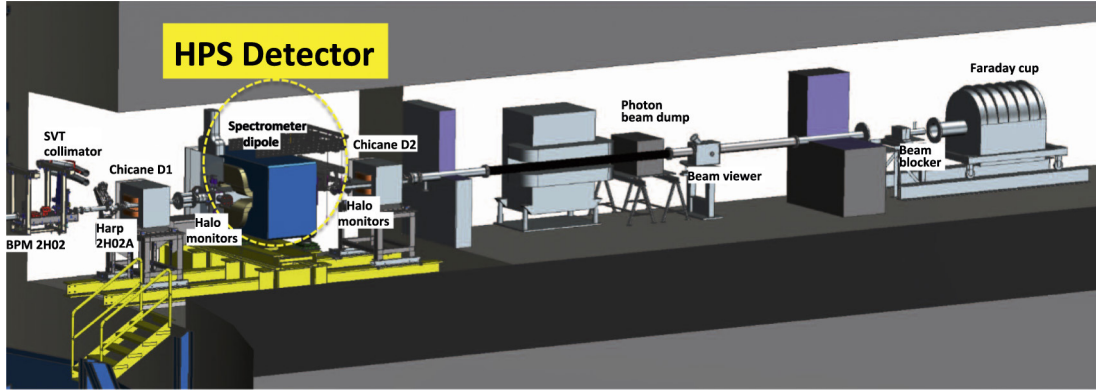


Figure 1.6: A schematic of the HPS beamline inside the Hall B alcove.

is required have a width less than $50\mu\text{m}$ with minimal beam tails and a mean within $50\mu\text{m}$ of the midplane between the top and bottom halves of the SVT. However, a beamspot as small as possible is desired as a smaller spot size will aid the constraint of vertices to the beamspot, thus improving the displaced vertex analysis by more efficiently rejecting tracks and vertices that are inconsistent with the beamspot. The beamspot size and position in the x -direction is less important since the resolution is far worse due to the fact that the SVT strips are oriented horizontally, so a width of less than $150\mu\text{m}$ is sufficient. An example of a wire scan measurement from the 2016 Engineering Run is shown in Fig. 1.7.

The SVT wire scans are unable to effectively measure the beam halo - beam electrons that differ significantly from the standard gaussian beam profile. This is important to understand for the purposes of long term radiation damage in the SVT. A measurement of beam halo from the 2015 Engineering Run by measuring occupancies in layer 1 of the SVT without the target is shown in Fig. 1.8. The beam halo intensity is $\sim 10^5$ which is sufficiently below the rate due to elastically-scattered beam electrons in the target, and thus is acceptable for HPS.

The chicane contains a single 18D36 analyzing magnet (or central magnet of pair spectrometer) with a pole length of 91.44 cm and a gap size of $45.72 \times 15.24\text{ cm}^2$. The analyzing magnet operated with a maximum field strength of 0.24 T for the 2015 Engineering Run and 0.50 T for the 2016 Engineering Run (the field strength scales linearly with beam energy and a maximum field strength of 1.5 T). In addition, two H-dipole Frascati magnets are set on either side of the analyzing magnet such that the total $\int \vec{B} \cdot d\vec{l}$ for the chicane system is 0 (each Frascati magnetic is half the analyzing magnet with opposite sign) which ensures the beam trajectory downstream of the chicane is independent of whether or not the chicane is powered.

The vacuum box has flanges upstream of the analyzing magnet for penetration of linear motion systems, cooling lines, and power and signal cables. The HPS target can be moved remotely by a linear shift from a stepper motor on the vacuum flange and is cantilevered at a ceramic support

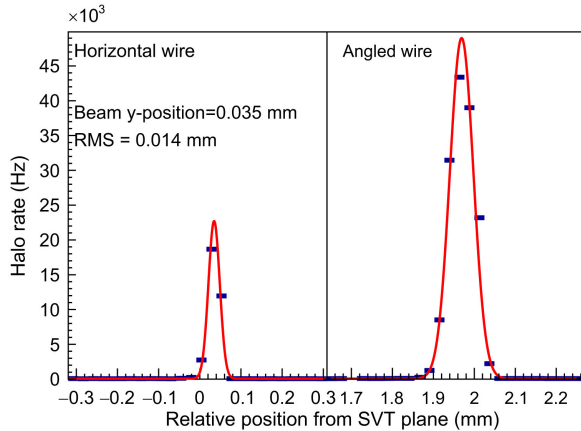


Figure 1.7: An example of an SVT wire scan measurement from the 2016 Engineering Run. This provides a measurement of the beam profile as close to the target as possible. This scan shows a beam with a $14 \mu\text{m}$ width in the y -direction with minimal tails and $35 \mu\text{m}$ from the nominal beam plane. This is an excellent beam profile for HPS.

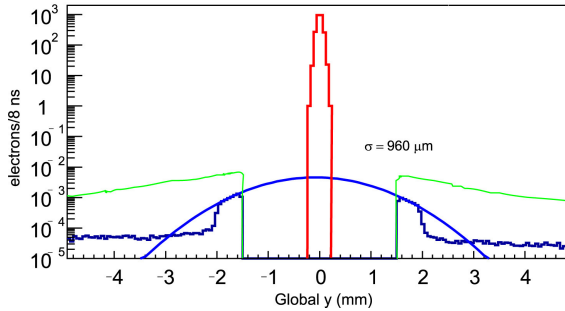


Figure 1.8: A measurement of the beam halo from 2015 Engineering Run using the occupancy of the first layer of the SVT in a no target run. The beam halo shows a width of $960 \mu\text{m}$ and 5 orders of magnitude less than the peak of the beam.

300 rod. There are several target options that can be selected based on the linear position of the target
 301 mount - $4 \mu\text{m}$ tungsten (0.125% radiation length design and 0.223% radiation length measured), 8
 302 μm tungsten (0.25% radiation length design and 0.116% radiation length measured), and a carbon
 303 target for calibration. The Ecal is downstream of the analyzing magnet. More details of the Hall B
 304 and HPS beamlines can be found in the HPS Beamlne paper [3].

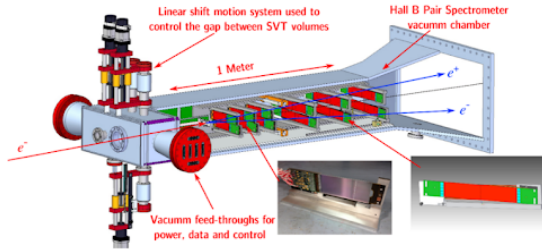


Figure 1.9: A schematic of the HPS silicon vertex tracker (SVT) which includes 6 layers of silicon microstrip sensors inside a vacuum and a uniform magnetic field. **Maybe find a better picture.**

305 1.3 Silicon Vertex Tracker

306 The silicon vertex tracker (SVT) provides a momentum measurement from charged particle trajectories
 307 that bend in the uniform magnetic field that can be used to reconstruct a vertex position.
 308 The SVT is an array of silicon microstrip sensors consisting of six layers (or measurement stations).
 309 Microstrips provide a 1D measurement along the direction of the sensor extending away from the
 310 beam. In order to provide a 3D measurement, each layer contains two components - an axial sensor
 311 with strips parallel to the beam plane and a stereo sensor rotated at a small angle. A large stereo an-
 312 gle would provide improved hit resolution in the direction along the axial strip, and hence improved
 313 momentum resolution.¹ However, a large stereo angle would also cause the stereo sensors to dip
 314 significantly into the beam plane, lose acceptance, and be prone to ghost hits (falsely reconstructed
 315 3D hits). Thus, the stereo angle is intentionally small and designed to be 0.100 mrad for the first
 316 three layers and 0.050 mrad for the last three layers, to provide a compromise between these affects
 317 and hit resolution. The axial/stereo sensor pairs reconstruct a 3D hit position at each of the six
 318 layers that are used for track finding.

319 The SVT is split into top/bottom halves to avoid the very high flux of electrons near the beam
 320 plane due to the “wall of flame”. Both the top and bottom halves are designed at a 15 mrad
 321 opening angle with respect to the primary. This opening angle must be as small as possible in order
 322 to capture as many A' s as possible which are typically highly boosted with a small opening angle.²
 323 The last three layers of the SVT are double wide (i.e. two sensors end to end) to increase acceptance
 324 for charged particles that are bending due to the uniform magnetic field.

325 The six layers are arranged such that the distance between the first and second layer (layer 1
 326 and layer 2) and the second and third layer is about 10 cm. The distance between the remaining
 327 layers is about 20 cm. Layer 1 is placed as close to the target as possible at about 10 cm in order
 328 to provide the best possible vertex resolution, and subsequently the second layer is placed close to
 329 the first layer to maximize pointing resolutions of tracks back to layer 1. The limiting factor of the

¹The resolution in the bend plane is simply the resolution in the non-bend plane divided by the stereo angle.

²This becomes even more critical for displaced A' 's which, for a given opening angle, lose acceptance rapidly as the decay vertex increases along the beam direction.

first layer placement is the fact that the sensors cannot be closer to $500 \mu\text{m}$ from the beam plane in order to avoid significant radiation damage from both elastically scattered electrons in the target and beam tails. Thus for a given opening angle of 15 mrad, the closest the first layer can be placed is $\approx 1.5 \text{ mm} / 15 \text{ mrad} = 10 \text{ cm}$.³ This approaches the maximum allowed occupancy for the silicon sensors of $\sim 1 - 2\%$. The sensors are designed to be as thin as possible to reduce the material budget and hence the effects due to multiple scattering. A summary of the some of the important design features of the SVT is shown in Table 1.1.

Layer Number	1	2	3	4	5	6
Distance z from target (mm)	100	200	300	500	700	900
Dead Zone Distance y (mm)	± 1.5	± 3.0	± 4.5	± 7.5	± 10.5	± 13.5
Number of Sensors	4	4	4	8	8	8
Stereo Angle (mrad)	100	100	100	50	50	50
Bend Plane Resolution (μm)	≈ 60	≈ 60	≈ 60	≈ 120	≈ 120	≈ 120
Non-Bend Plane Resolution (μm)	≈ 6	≈ 6	≈ 6	≈ 6	≈ 6	≈ 6
Material Budget ($\%X_0$)	0.7%	0.7%	0.7%	0.7%	0.7%	0.7%
Module Power Consumption (W)	6.9	6.9	6.9	13.8	13.8	13.8

Table 1.1: A summary of the basic parameters for different layers in the SVT.

³The next subsection described a 1 mm inactive part of the sensor, so the active region begins at 1.5 mm from the beam plane.

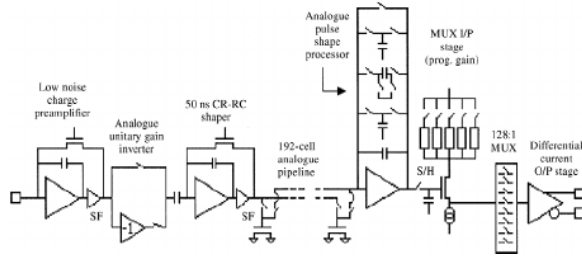


Figure 1.10: A schematic of the APV25 deep submicron readout chip that was originally designed for CMS detectors but is used for the HPS SVT.

³³⁷ 1.3.1 Sensors and Readout

³³⁸ HPS utilizes the silicon microstrip sensors originally designed and procured for the upgraded DØ
³³⁹ detector at Fermilab for run IIb, which was cancelled in favor of an insertable Layer 0. The sensor
³⁴⁰ technology was chosen to minimize material budget to mitigate multiple scattering effects and to
³⁴¹ be highly tolerant to radiation. These sensors are single-sided p+n with AC-coupled readout with
³⁴² a bulk that is lightly doped n-type silicon. The strip implants are strongly p-type doped. The bias
³⁴³ of the strips comes from polysilicon resistors at the end of the strips which are capacitively coupled
³⁴⁴ to aluminum readout strips that run on top of the silicon strips.

³⁴⁵ The sensor cut dimensions are 100 mm × 40.34 mm with an active area of 98.33 mm × 38.34 mm.
³⁴⁶ The silicon strip pitch is 30 μm ; however, only every other strip is readout (i.e. the readout pitch is
³⁴⁷ 60 μm). When a particle is incident on an intermediate strips (a sense strip), the charge will split
³⁴⁸ between the neighboring readout strips and this charge sharing will improve single hit resolution.
³⁴⁹ Each sensor has 640 readout strips.

³⁵⁰ The useful sensor lifetime is limited by radiation damage where the sensor strips closest to the
³⁵¹ beam plane are expected to undergo a large electron flux of $> 10^{15}$ electrons per cm^2 over the
³⁵² duration of the experiment. Specifically, incident particles can displace silicon nuclei from their
³⁵³ crystal lattice which causes an effective type inversion, where the n-type bulk is converted to p-type.
³⁵⁴ The radiation damage leads to an increase in depletion voltage which means the charge collection
³⁵⁵ efficiency for a given bias voltage will decrease. Thus as a sensor undergoes radiation damage over
³⁵⁶ the course of the run which is highly non-linear and concentrated on the middle beam edge of the
³⁵⁷ sensor (mostly from elastically scattered beam electrons in the target), the bias voltage must be
³⁵⁸ increased to keep the same charge collection efficiency. Eventually, this bias voltage will approach
³⁵⁹ the breakdown voltage and will no longer be usable in the experiment. In addition, radiation damage
³⁶⁰ leads to increased leakage current, and thus sensor heating. For these sensors, the nominal operating
³⁶¹ bias voltage is 180 V. The design specifications required a breakdown voltage greater than 350 V;
³⁶² however, only sensors with a breakdown voltage greater than 1000 V were used. For the 2015 and
³⁶³ 2016 Engineering Runs, radiation was not an issue.

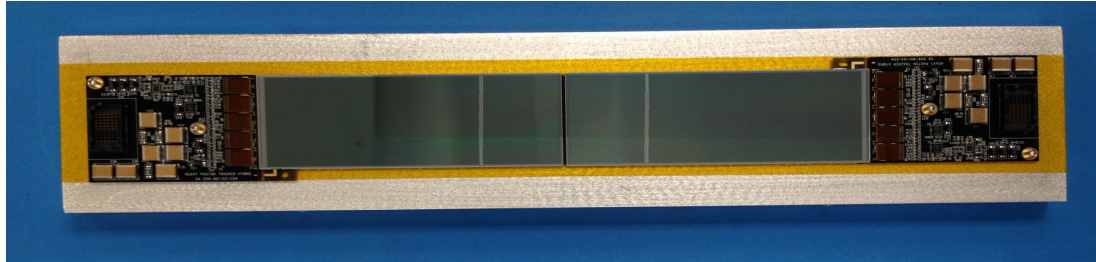


Figure 1.11: A picture of the two SVT sensors (end to end) with each sensor. The sensors are readout by APV25 chips which are housed on a hybrid circuit.

These sensors are readout by the APV25 readout chip which was developed for the silicon microstrip sensors in the CMS tracker [14] [8]. A schematic is shown in Fig. 1.10. The APV25 chip has high hit time resolution and has the ability to readout multiple consecutive samples of its shaper waveform, thus it is useful for pileup rejection - an essential requirement for HPS. The APV25 chip has 128 input channels, thus each sensor has $640 / 128 = 5$ readout chips. Each channel contains a charge-sensitive preamplifier with an optional inverter, CR-RC shaper, and a 192-cell-deep analog pipeline. Only 160 out of 192 of these cells are used to buffer samples and the remaining 32 cells buffer the addresses of samples waiting to be readout. A picture of two SVT sensors with APV25 chips is shown in Fig. 1.11.

The clock is designed for a clock period of 25 ns which is equivalent to the LHC bunch crossing. However, HPS adapted this chip to run on a clock period of 24 ns (41.6 MHz) since it is an even multiple of the both the JLab and Ecal clocks, which are 2 ns and 4 ns, respectively. Each channel samples the shaper output and stores it in a cell of its pipeline on each clock. Once a trigger is received, the pipeline cell of each channel is readout, and the chip multiplexes the 128 signals onto a single differential current output. A configurable latency (the distance between the read and write pointers) setting determines which pipeline cells are readout.

The samples are readout by the Analog Pulse Shape Processor (APSP) which has the ability to operate in two distinct modes - deconvolution mode and multi-peak mode. For each trigger signal, The deconvolution mode allows for three consecutive pipeline cells to be readout and combined into a weight sum whereas the multi-peak readout mode allows for three consecutive pipeline cells to be readout without any additional operations. In order to mitigate pile-up effects from large occupancy, HPS is operated in multi-peak readout mode and for each trigger, the APV25s are sent two consecutive trigger signals for a total of six samples. These six samples are fit to a pulse shape predetermined from offline calibration and reconstructed offline in order to obtain the pulse amplitude and hit time. This is described in detail in Sec. ??.

During the 2015 Engineering Run, the nominal settings of the APV25 were utilized. For the 2016 Engineering Run, these same parameters were used with the exception of the input parameters of the pulse shaper which were optimized to have a sharp rise time for optimal time resolution and

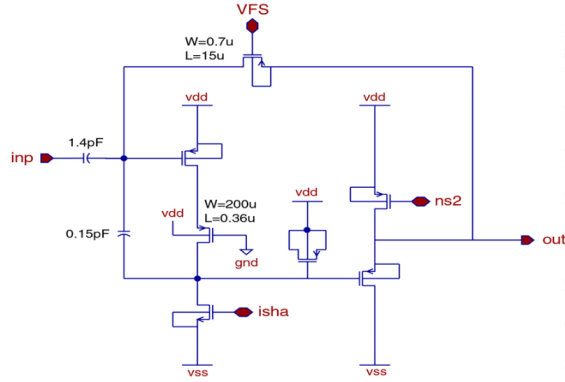


Figure 1.12: The APV25 Shaper schematic. The parameters VFS (related to the input voltage) and isha (related to the input current) were optimized for improved time resolution and reduced pileup.

³⁹² quick fall time to further reduce pileup effects. A schematic of the APV25 shaper and the parameter
³⁹³ which were optimized is shown in Fig. 1.12.

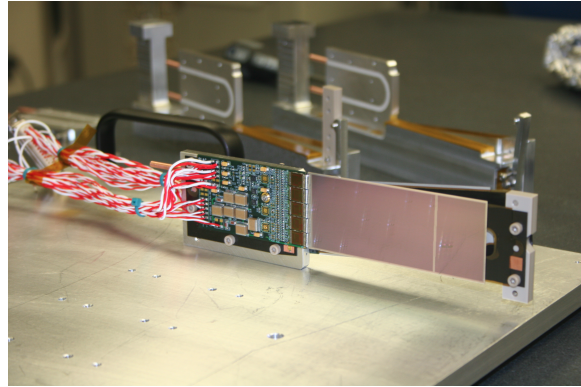


Figure 1.13: A single SVT module which comprises of two silicon microstrip sensors which are axial (front) and stereo (back) to the beam plane. Each sensor is supported by a carbon fiber support structure can be seen protruding from the right of the axial sensor.

³⁹⁴ 1.3.2 SVT Mechanicals

³⁹⁵ Each sensor is part of a base unit referred to as a “half-module” and is comprised of a single or
³⁹⁶ double sensor, carbon fiber support structure, and hybrid readout circuit boards. The first three
³⁹⁷ layers 1-3 are composed of a single sensor and hybrid while the last three layers 4-6, since they are
³⁹⁸ double wide, are composed of double sensors and hybrids. Each of these half-modules can be used
³⁹⁹ as the axial or stereo components of the detector.

⁴⁰⁰ The carbon fiber, in addition to support for the sensor, acts as ground plane for the half-module
⁴⁰¹ while a layer of Kapton insulation isolates the carbon fiber from the back of the sensor which is
⁴⁰² at high voltage. The Kapton and carbon fiber are kept as thin as possible, much thinner than the
⁴⁰³ silicon sensors, to avoid adding additional unnecessary material that increases multiple scattering in
⁴⁰⁴ the tracker.⁴

⁴⁰⁵ The hybrid circuit boards house the APV25 readout chips, five per half module, and provides
⁴⁰⁶ a connection of the sensor to the rest of the DAQ. The APV25 power, control lines, and output
⁴⁰⁷ channels are wirebonded to the hybrid while the input channels are wirebonded directly to the
⁴⁰⁸ sensor. The hybrid contains temperature sensors and carries filter capacitors for the sensor bias.

⁴⁰⁹ Two of these half-modules are paired to create a module with one axial and one stereo half-
⁴¹⁰ module. The axial half-modules are parallel to the beam plane and the stereo half-modules are
⁴¹¹ rotated at a small angle and dips into the beam plane on the positron side (beam left, the side
⁴¹² opposite to where beam background is bent). These modules are mounted on aluminum support
⁴¹³ modules which hold the half-modules from both sides and, in addition to mechanical support, these
⁴¹⁴ supports also pull heat generated by the hybrids. The half-modules and the support undergo thermal
⁴¹⁵ contraction at different rates, thus the module support applies a constant tension from a spring pivot

⁴A window was machined into the carbon fiber support such that the material in the middle of the sensor, where most of the physics of interest is expected, is further minimized.

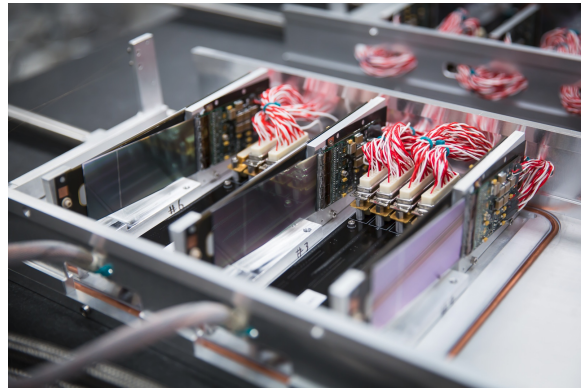


Figure 1.14: Layers 1 - 3 modules of the SVT (from left to right) are placed in one of the U-channels. Copper cooling lines and electrical lines can be seen. The wire frames and scan wires can also be seen on the left.

416 in order to keep the half-modules flat at operating temperature ($\sim 0^\circ \text{ C}$). A picture of a complete
 417 module is shown in Fig. 1.13.

418 Three of these modules are mounted on an aluminum support structure called a “U-channel”.
 419 The SVT contains a total of four of these U-channel for each top and bottom of L1-3 and L4-6
 420 (which are larger). Each U-channel is supported by the kinematic mounts which guarantee reliable
 421 and repeatable positioning when the U-channels are installed and re-installed. The L1-3 U-channels
 422 rest on two downstream kinematic mounts, which act as a hinge, and is supported at the upstream
 423 end by motion levers which guide the L1-3 U-channels towards and away from beam. Finally, the
 424 L1-3 modules house scan wires as close to the target position as possible to measure the beam
 425 position and profile relative to the SVT to assess beam quality. Each U-channel has two wires -
 426 one parallel to the beam plan and one rotated at a slight angle - in order to obtain 2D position
 427 information. A picture of a L1-3 U-channel is shown in Fig. 1.14.

428 The SVT underwent a mechanical survey before installation using a coordinate-measuring ma-
 429 chine which utilized both optical and touch probe measurements to locate 3D target points. The
 430 survey ensures the SVT was assembled as designed and allows adjustment for the adjustable com-
 431 ponents if necessary, and it provides an initial alignment for track reconstruction whose quality
 432 depends strongly on precise knowledge of the sensor positions and orientations. This is sufficient
 433 for initial knowledge, but the sensor is later aligned using the data as described in Sec. 2.7. Lastly,
 434 the survey provides a measurement of the edge of the L1 axial sensor relative to the wire on the
 435 U-channel to ensure that the sensor edge is placed at $500 \mu\text{m}$ from the beam plane. A picture of the
 436 SVT installed in the SVT vacuum box is shown in Fig. 1.15.

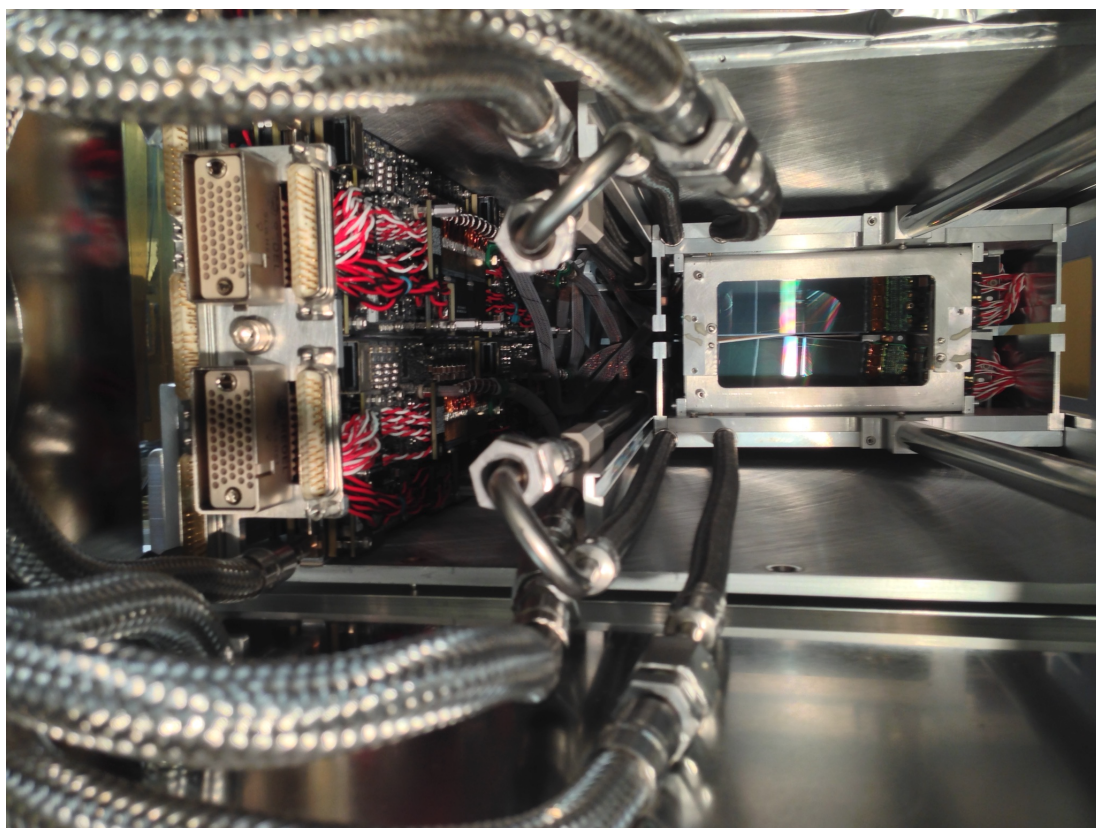


Figure 1.15: A picture inside the SVT vacuum chamber with everything installed except for the target. The frontend boards (FEBs) and FEB cooling plate are on the left. The SVT cooling lines protrude outward in the picture. The first layer of the SVT can be seen in the back behind the wire frames. The SVT is in its closed position and the beam must go through the 1 mm gap between the top and bottom sensors.

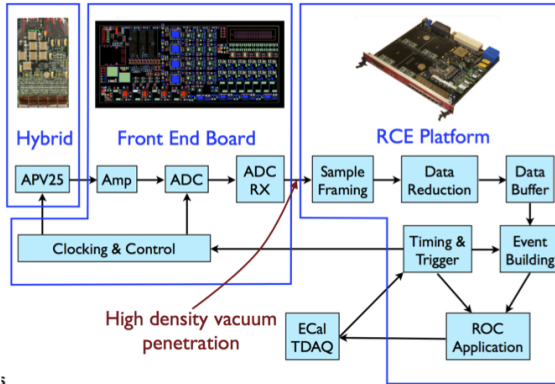


Figure 1.16: A schematic of the SVT DAQ system described in Sec. 1.3.3.

437 1.3.3 SVT Data Acquisition, Power, and Services

438 HPS must have a method to pass power and data to the detector given the constraints of the detector
 439 design as described previously. In addition, the nearest rack that can contain the data acquisition
 440 (DAQ) and power supplies is located about 20 m from where HPS is installed thus requiring the
 441 analog signals from the APV25 readout chips to be converted to optical digitized signals. As a
 442 result, the signal digitization and low-voltage regulation is performed inside the vacuum on front end
 443 boards (FEBs) located on a cooling plate alongside the SVT. And because the SVT and front end
 444 boards (FEBs) are in vacuum, all power and DAQ must pass through a pair of 8-inch vacuum flanges
 445 upstream of the dipole magnet, thus requiring the reduction of the number of signals.

446 Each of the 10 FEBs can service either a pair of L1-3 modules or a single L4-6 modules totalling
 447 four hybrids which is connected by a single bundle of impedance-controlled twisted pair magnet wire
 448 (which reduces crosstalk and electromagnetic interference between the lines). This carries the analog
 449 APV25 output signals, digital controls, trigger signals, low-voltage power, and high-voltage sensor
 450 bias. The data and control signals are carried by a mini-SAS cable on a high-speed data link. The
 451 FEBs digitize the output signals from 20 APV25 chips (4 hybrids \times 5 APV25 chips). A preamplifier
 452 on the APV25 converts a differential current signal to voltage and is digitized to a value between
 453 0 and 16384 by an AD9252 14-bit analog to digital converter (ADC) which samples the signal at
 454 41.667 MHz.⁵ Each FEB contains a Xilinx Artix-7 FPGA that sends the ADC data upstream to
 455 multi-gigabit receivers and controls and monitors the hybrid state and configuration.

456 The digitized data, low-voltage power, and high-voltage bias from the FEBs is transferred to
 457 electronic boards on the penetration of the vacuum flange (called “flange boards”) through mini
 458 SAS cable for data and twisted pair cables for power and bias.⁶ There are two flange boards on

⁵The 14-bit samples for each of the 23040 APV25 channels is too much data to store. The DAQ requires a readout threshold of three out of six samples above a threshold (three times the channel noise above the mean) that is predetermined from offline calibration.

⁶The flange boards are custom-made since the number of required connections is too high for conventional vacuum

459 the beam right side - one for high voltage and the other for low voltage. The four flange boards
460 located on the beam left side convert the digitized signal to optical using fiber transceivers so the
461 signal can be transferred a large distance to the general-purpose Reconfigurable Cluster Elements
462 (RCE) platform. The RCE plafrom was developed at SLAC and is housed in a standard Advanced
463 Telecommunications Computing Architecture (ATCA) crate. The data from the FEBs is distributed
464 on a Cluster on board (COB) between two ATCA blades housed inside the crate. Each COB contain
465 8 RCE processing nodes which use Xilinx Zynq-7000 series FGPAs to apply data reduction to signals
466 from the flange boards and build events.

467 Each COB houses several generic hardware daughterboards common to RCE platforms including
468 four Data Processing Modules (DPM) and one Data Transport Module (DTM). The DPMs process
469 and reduce data at high speed while the DTM is responsible for timing and trigger distribution.
470 The only HPS-specific hardware on the COB is the Rear Transition Module (RTM) which interfaces
471 the optical fibers from the signal flange boards to the COB. The SVT DAQ utilizes a total of two
472 COBS and two RTMs. In addition to the core of the DAQ, the rack also contains the low and high
473 voltage Wiener MPOD power supplies which are commonly used for a variety of JLab experiments.
474 A schematic of the SVT DAQ system is summarized in Fig. 1.16.

475 The SVT services - motion, cooling, and power - are supplied from outside the vacuum through
476 several flanges located upstream of the vacuum chamber. The SVT is cooled through 2 independent
477 cooling loops one for the silicon sensors and the other for the FEBs. The silicon sensors must be kept
478 below 0° C in order to avoid further radiation damage due to higher temperature (called reverse
479 annealing). They are cooled through a hydrofluoroether compound circulating through copper lines
480 embedded into the U-channels where top and bottom are split and L1-L3 and L4-L6 are connected
481 in series. The specialized fluid is necessary since its low viscosity maintains high flow rates at low
482 temperatures.

483 The FEBs only need to be kept at around room temperature while dissipating only the heat the
484 produced from operating the FEBs themselves. Thus, distilled water is sufficient as a cooling fluid
485 and is circulated through copper lines embedded in the FEB cooling plate. The FEBs themselves
486 are cooled through direct thermal contact with the cooling plate. A picture of the FEBs on the
487 cooling plate is shown in Fig. 1.17.

488 In addition to cooling components, there are three linear shift stepper motors that provide
489 independent motion control of the top and bottom U-channels as well as the target frame. The
490 motors are powered and controlled by a Newport XPS controller. All three motors have both a
491 hardware and software safety stop, while the two motors that control the U-channel linear motion
492 also include a precision limit switch to ensure the SVT is not accidentally driven into the beam.



Figure 1.17: The FEB cooling plate complete with 10 FEBs fastened to the front and back of the plate.

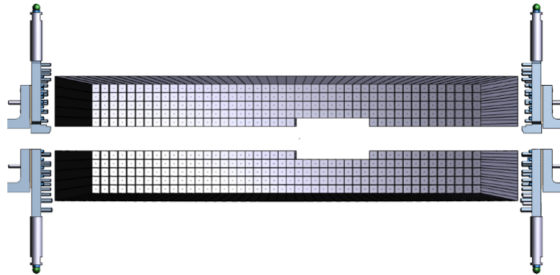


Figure 1.18: A rendering of the HPS Ecal. Each segment is one of the 442 lead tungstate crystals and the Ecal is split in half to avoid radiation damage from the most intense parts of the beam.

493 1.4 Electromagnetic Calorimeter and Trigger

494 The electromagnetic calorimeter (ECal) is an array of 442 lead tungstate scintillating crystals
 495 (PbWO_4) and is used primarily for precision timing and triggering (cite). The crystals are reused
 496 from the CLAS Inner Calorimeter (IC). The crystals have front faces of size $1.3 \times 1.3 \text{ cm}^2$, are 16
 497 cm long, and are tapered such that the back faces have dimensions $1.6 \times 1.6 \text{ cm}^2$ for acceptance
 498 purposes. The Ecal itself is split into top and bottom halves much like the SVT to avoid the most
 499 intense parts of the beam plane. Each half contains 5 rows of 46 crystals with the exception of the
 500 removal of 9 crystals in the innermost row to avoid large occupancy from beam background. This is
 501 referred to as the Ecal hole or electron gap. The innermost rows are positioned 2 cm from the beam
 502 plane to maintain the 15 mrad design opening angle. The face of the Ecal is positioned 139.3 cm from
 503 the target position. Each crystal is readout by an avalanche photodiode (APD) on the back face of
 504 the crystal (specifically, a Hamamatsu S8664-1010 APD). One blue and one red LED are positioned
 505 on the front face of each crystal and are used for monitoring purposes (specifically radiation damage
 506 and stability of readout gain). Since the scintillator response is temperature-dependent, the Ecal is
 507 surrounded by a thermal enclosure.

508 The primary purpose of the Ecal is the main trigger. Jefferson Laboratory has developed general-
 509 purpose readout boards called the FADC250 digitizer boards, or simply FADC. Each Ecal crystal
 510 contains a preamplifier that outputs signals through a motherboard. Each FADC board has 16 input
 511 channels and are continuously digitized at 250 MHz to a 12-bit precision which are then stored in
 512 8 μs deep pipelines to await being readout if a trigger signal is received. There are several readout
 513 modes available, but HPS utilizes the readout mode that outputs a window of 100 samples that
 514 allows pulse fitting with optimal time resolution.

515 The FADC boards are located in VXS crates also developed by Jefferson Laboratory as a general-
 516 purpose trigger framework. An algorithm that continuously looks for threshold crossings and in-
 517tegrates the digitized signal from the FADC within a fixed window converts the integration to an
 518 energy from previously calibrated values from cosmic rays. This gives a crystal position, energy, and

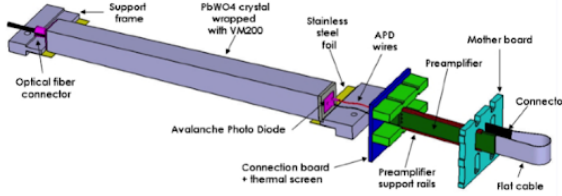


Figure 1.19: A schematic of a PbWO_4 crystal in the Ecal.

time of the threshold crossing which are then passed to the Global Trigger Processor (GTP) every 32 ns. Each Ecal half has a GTP board which clusters hits by looking at a 3×3 block around a center crystal with a least a 50 MeV (Is this number still accurate??) and the surrounding hits within 16 ns of the center hit. This defines a cluster with a center crystal, hit time, number of hits, and total energy. Each GTP reports these clusters to the Single Subsystem Processor (SSP) board.

The SSP uses these clusters to make a decision on the Trigger. For the 2016 Engineering Run, we have 5 triggers. The first is a “pulser” trigger which fires at a fixed rate of 100 kHz. Next, there are two triggers that fire on single clusters that are called “singles1” and its corresponding trigger which has looser requirements “singles0”. Finally, there are two triggers that fire on a pair of top-bottom clusters (at least one cluster in each GTP). These are called “pairs1” and “pairs0” triggers, where pairs0 is the looser version of pairs1. The pairs1 is our nominal trigger that is used for the physics analysis. In order to prevent the other triggers from triggering at a rate higher than the DAQ can handle, the singles triggers and the pairs0 trigger are prescaled such that one trigger in 2^n triggers are accepted where n is in the range of 10 to 13.

Once the SSP makes a trigger decision, if a cluster or pair of clusters meets the requirements above a trigger is sent to the Trigger Supervisor board (TS) and distributes the trigger to the Trigger Interface (TI) boards. The TS can reject the trigger if a subsystem is not ready to accept a trigger or the trigger follows too closely to another trigger.

The livetime of the DAQ, that is the fraction of time the DAQ is willing to receive triggers, must be understood in order to properly normalize the data. One way to measure the livetime is to use the pulser trigger. Since the pulser trigger fires at a constant rate, the ratio of the number of pulser triggers recorded to the number of pulser triggers that should have been recorded based on the 100 Hz rate is a direct measurement of the livetime. Another way to measure the livetime is to combine the measurement of integrated charge from the Faraday cup as described in Sec. 1.2 with a measurement of the integrated charge with the DAQ live. This is called the “gated Faraday cup scaler”, and the ratio of this scalar to the total integrated charge is the DAQ livetime. What do we actually use for 2016?

The HPS physics trigger is designed to maximize efficiency for A' s, or more generally e^+e^- pairs near the beam energy, while sufficiently suppressing backgrounds to avoid overwhelming the DAQ

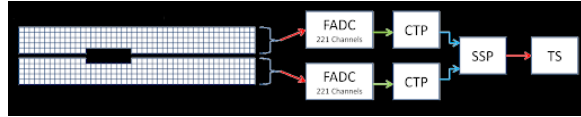


Figure 1.20: A schematic of the trigger for the Ecal. Top and bottom halves of the Ecal are each readout by FADC readout boards, and then sent to the SSP where a trigger decision is made.

systems. The most significant one-cluster background is elastically-scattered electrons in the target. Thus a trigger requiring at least two clusters will eliminate a large fraction of these. The largest source two-cluster backgrounds is elastically-scattered electrons in the target in coincidence with wide-angle bremmstrahlung. These can be eliminated by first requiring top and bottom coincident clusters as well as further timing and energy cuts.

The time coincidence between top and bottom clusters are required to be within 12 ns and is corrected for time walk. In addition to timing requirements, there is a coplanarity requirement that requires two clusters on opposite sides of the beam axis. It is intended to select only e^+e^- coincident pairs which are expected on average to be symmetric about the beam axis. The azimuthal angle ϕ relative to the beam axis of the top and bottom cluster is required to be within $\pm 30^\circ$ of 180° .

Furthermore, the trigger requires some basic energy requirements. First, a maximum energy sum requirement eliminates a large fraction of coincident beam scattered electrons. For the minimum energy requirements, it is important to note that there are substantial energy losses from a variety of sources in the Ecal such as the absorption of energy by the vacuum flange, gaps between crystals, or the back of the Ecal. As stated previously, this is accounted for in the reconstruction by detailed MC studies, but is not accounted for in the trigger. In addition, particles can hit the innermost row of the Ecal and lose energy where much of the shower is lost in the beam gap. This is especially important since a large fraction of signal, particularly at lower mass due to the smaller opening angle, occurs at the beam edge of the calorimeter. For this reason, there are only loose requirements on the minimum energy on individual clusters and minimum energy sum that are below the truth energy threshold of what one would expect from an A' .

Finally, it is expected that the lower energy decay particles from A' 's will have be further from the beam axis due to increased bending of the lower momentum particle from the magnetic field. The energy-distance cut rejects particles that are both low energy and close to the beam axis. This cut has the effect of first rejecting wide-angle bremsstrahlung which is a photon that is typically lower energy and closer to the beam axis and second, rejecting beam electrons that scrape the Ecal edge where most energy is lost. The cut is based on the cluster energy E_{low} and the cluster distance from the beam axis r_{low} and is expressed as $E_{low} + (5.5 \text{ MeV / mm}) r_{low} > 0.7 \text{ GeV}$.

The pairs1 trigger requirements - including the timing, cluster energy, cluster size, energy sum, cluster energy difference, coplanarity, and energy-distance requirements - are summarized in Table 1.2.

Trigger Description	Value
Time Difference	$ t_{top} - t_{bot} \leq 12$ ns
Cluster Energy	$0.15 < E < 1.4$ GeV
Cluster Size	$N_{hits} \geq 1$
Energy Sum	$0.6 < E_{top} + E_{bot} < 2.0$ GeV
Energy Difference	$ E_{top} - E_{bot} < 1.1$ GeV
Coplanarity	$ \phi_{top} - \phi_{bot} - 180^\circ < 35^\circ$
Energy-Distance	$E_{low} + (5.5 \text{ MeV / mm}) r_{low} > 0.7 \text{ GeV}$

Table 1.2: Summary of the pairs1 Trigger Selection from the 2016 Engineering Run.

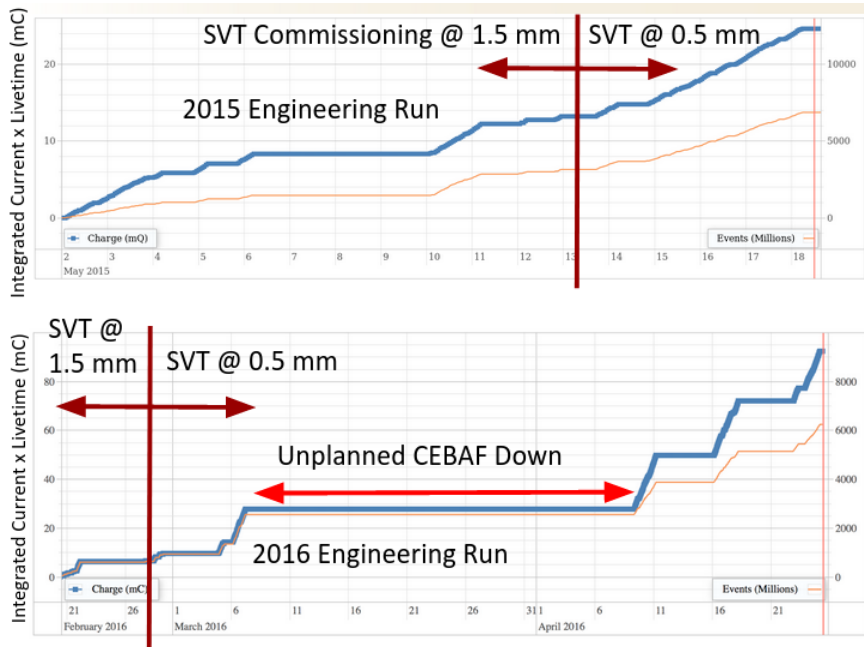


Figure 1.21: A summary for the integrated charge over time for the Top: 2015 Engineering Run and Bottom: 2016 Engineering Run. **Replace these figures**

579 1.5 Datasets

580 To date, HPS has three data taking runs - an engineering run in 2015, and engineering run in 2016,
 581 and a physics run in 2019. The 2015 engineering run was taken with a beam energy of 1.056 GeV
 582 and beam current of 50 nA incident on a $4 \mu\text{m}$ target. The total luminosity taken over opportunistic
 583 nights and weekends amount to 74.72 nb^{-1} which corresponds to 0.4671 mC of charge and 0.1
 584 PAC days. A broken cryogenic helium liquifier (CHL) shortly before the run began resulted in the
 585 operation of only a single CEBAF linac for this run (as opposed to the usual two linacs). This gave
 586 HPS a unique opportunity to run at this beam energy equivalent to half a pass which would have
 587 otherwise been unavailable.

588 The 2016 Engineering Run was taken with a beam energy of 2.3 GeV and beam current of 200 nA
 589 incident on a $8 \mu\text{m}$ target. The total luminosity taken over weekends amount to 10753 nb^{-1} which
 590 corresponds to 0.4671 mC of charge and 5.4 PAC days. **The luminosity need to be checked.** Much
 591 of the analysis is performed on a blinded $\sim 10\%$ sample (1101 nb^{-1}) before the final results over the
 592 whole dataset are produced. The data for the 2016 Engineering Run was collected by running on
 593 weekends over the span of several months.

594 A summary of the accumulated luminosity over time for the 2015 and 2016 Engineering Runs is
 595 shown in Fig. 1.21. The focus of this thesis is the displaced vertex analysis from the 2016 engineering
 596 run. The 2019 Physics Run was take with upgrades and is described in Sec. ??.

597 **Chapter 2**

598 **Event Reconstruction & Selection**

599 Reconstruction is the process in a given event of building actual physics processes, such as an A'
600 decay, from the raw hits of the detector channels readout by the trigger. The HPS event reconstruc-
601 tion is based on the lcsim software toolkit [10] and uses both reconstructed clusters from the Ecal
602 and tracks from the SVT, which are done independently until Ecal clusters and tracks are matched
603 by extrapolating the track state at the last layer of the SVT to a cluster in the Ecal for particle
604 identification. These objects, mainly e^+e^- pairs or e^-e^- pairs, are used to reconstruct vertices used
605 for the physics analysis. The multiple stages of the HPS reconstruction - SVT hit reconstruction,
606 tracking, vertexing, and Ecal clusters - are as follows in the proceeding sections.

607 **2.1 HPS Coordinate Systems**

Coordinate System	<i>x</i>	<i>y</i>	<i>z</i>
JLab Coordinates	Beam left	Vertical	Beam direction
Detector/HPS Coordinates	Beam left rot. -30.5 mrad	Vertical	Beam direction rot. -30.5 mrad
Tracking/lcsim Coordinates	Beam direction	Beam left	Vertical

Table 2.1: Basis for several different coordinate systems used in the HPS reconstruction and analysis.

608 The HPS coordinate system is defined globally by the Hall B beamline where the the *x*-axis
609 points beam left in the bend plane, the *y*-axis points vertically upwards, and the *z*-axis points along
610 the direction of the beam. The origin is set at the intersection of the nominal beam and nominal
611 target position. Due to the asymmetry of HPS with respect to the chicane, where the beam is
612 rotated 30.5 mrad about the *y*-axis in the $-x$ -direction to the HPS beam axis. In other words, the
613 HPS beam axis is rotated by 30.5 mrad beam left from the Hall B beam axis due to the first dipole
614 magnet in the chicane. This is the natural reference frame for reconstructed particles and, unless

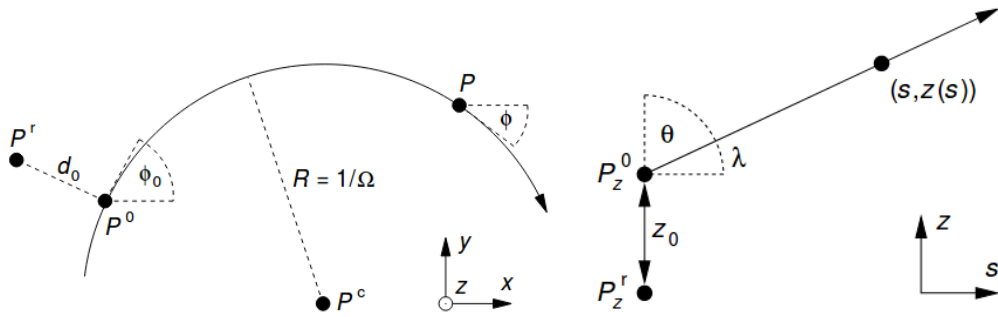


Figure 2.1: A schematic of the linear collider tracking parameters 2.1 [12].

otherwise stated, the physics analysis including positions and momenta will be performed in this frame.

The entire HPS SVT lies within a uniform magnetic field, thus a charged particle will form a helix. Unfortunately, the coordinate systems for track reconstruction and analysis on HPS are different. HPS utilizes perigee parametrization of tracks that fixes a magnetic field along the z -axis (which is the y -axis in HPS coordinates). The tracking coordinates are oriented approximately such that the x -axis points along the direction of the beam, the y -axis points beam left, and the z -axis points vertically upwards. In addition, each track is defined by 5 track parameters - Ω , d_0 , z_0 , $\tan\lambda$, and ϕ - and are briefly described below and shown in Fig. 2.1 [12].

1. Ω is the signed curvature of the track (i.e. the inverse of the radius $C = -q/R$).
2. d_0 is the signed impact parameter in the xy tracking plane. In the HPS detector frame, this translates to the impact parameter along the x (horizontal) direction.
3. z_0 is the tracking z position at the point of closest approach to the reference point. This is the key tracking parameter for the isolation cut. In the HPS detector frame, this approximately corresponds to the impact parameter in the y (vertical) direction.
4. $\tan\lambda$ is the slope of the straight line in the sz tracking plane. In the HPS detector frame, this translates to the slope of the track dy/dz in the yz plane.
5. ϕ is the azimuthal angle of the momentum of the particle at point of closest approach to the reference point.

Due to multiple scattering in the silicon sensors, different segments of the track (between each silicon plane) is describe by a different helix called track states. Thus each track segment will have its own set of unique 5 track parameters, and a track will have 11 or 13 track states depending on the number of hits on track. This process is described in Sec 2.3.3.

638 2.2 Ecal Reconstruction

639 The Ecal reconstruction is the process of building particle clusters from the waveforms readout in
 640 single crystals of the Ecal for a given event. Ecal crystals that are readout store 100 samples in 4
 641 ns intervals relative to the trigger time. The pulse shape is fit with a three-pole function

$$F_{3pole}(t) = \frac{t^2}{2\tau^3} e^{-\frac{t}{\tau}} \quad (2.1)$$

642 The time constant τ is calibrated offline for each channel and is typically ~ 2.4 ns. From this
 643 function, the pedestal, time of the pulse, and amplitude are fit in offline reconstruction and pileup
 644 fits are not considered. From the amplitude, the pulse is converted to energy by two types of channel
 645 calibrations - cosmic rays and elastic scatters in the target ([cite](#)). Cosmic rays are calibrated before
 646 data taking with the beam off through the detection of minimum ionizing particles (MIPs), which
 647 have a known rate of energy loss, passing downwards through the Ecal. After data taking, cluster
 648 energy is calibrated from elastically scattered electrons from the target, which are very near the
 649 beam energy, and the gain constants for every crystal is adjusted until the energies match what is
 650 observed in MC. Both cosmic ray MIPs and elastically scattered electrons populate the full range
 651 of interest in energy.

652 In order to form clusters in the Ecal, individual hits are formed together using a clustering
 653 algorithm adapted from the CLAS Inner Calorimeter [[cite](#)]. Hits with a local energy maxima are
 654 seeded for clusters, and then the algorithm searches for neighboring crystals with seeds or a hit on
 655 a cluster within 8 ns of the seed. The seed hit time is used as the time of the cluster with larger
 656 energy since higher energy hits have better timing resolution.

657 The energy of the cluster is initially the sum of the individual hit energies. However, this energy
 658 does not account for electromagnetic showers that are lost on the Ecal edges or energy absorbed
 659 in the vacuum flanges. In addition, particles generally enter an Ecal crystal at an angle off axis
 660 from crystal axis and electromagnetic showers deposit energies at all Ecal depths resulting in the
 661 fact that maximum energy deposition may not occur in the same crystal as the crystal whose
 662 front face the particle has traversed. As a result, energy corrections are based on detailed MC
 663 studies and the energy is corrected as a function of particle type (photon, electron, or positron),
 664 energy, and angle, where the particle type must be determined by track-cluster matching later in the
 665 reconstruction described in Sec. 2.4. In addition, the position of the cluster is initially determined
 666 by a logarithmically weighted centroid. For the same reason as energy, the position must also be
 667 corrected and is done so in the same MC studies as energy. [cite these MC studies](#)

668 2.3 SVT Reconstruction

669 The SVT reconstruction is the process of building particle tracks from the waveforms readout in
 670 single strips of the SVT for a given event. These tracks are used to form electron and positron
 671 objects (tracks matched with Ecal clusters), which are then used to form vertices used in the final
 672 analysis.

673 2.3.1 SVT Hit Reconstruction

674 For each trigger, SVT channels where at least three of the six samples are above the readout thresh-
 675 old, that was determined by offline calibration before data taking in calibration runs (for reasons
 676 described in Sec. 1.3.3), are readout. For each strip in the SVT that is readout, the APV25 reads
 677 out six samples of 24 ns intervals. The APV25 response is modeled as a four pole filter with three
 678 coincident poles (i.e. three of the poles with the same time constant). This gives the following
 679 transfer function with two time constants τ_1 and τ_2 .

$$\tilde{F}(\omega) = \frac{1}{(1 + i\omega\tau_1)(1 + i\omega\tau_2)^3} \quad (2.2)$$

680 The inverse Fourier Transform of this transform function is the pulse shape given by

$$F(t, \tau_1, \tau_2) = A \frac{\tau_1^2}{(\tau_1 - \tau_2)^3} \left(e^{-\frac{t-t_0}{\tau_1}} - \sum_{k=0}^2 \left(\frac{\tau_1 - \tau_2}{\tau_1 \tau_2} (t - t_0) \right)^k \frac{e^{-\frac{t-t_0}{\tau_2}}}{k!} \right) \quad (2.3)$$

681 The time constants are predetermined offline by fitting pulses in calibration runs and have typical
 682 values of $\tau_1 \approx 72$ ns and $\tau_2 \approx 12$ ns. t_0 is defined as the time the fit crosses 0 and is set as the time
 683 of the raw hit. A is related to the amplitude of the pulse in ADC counts. Both of these quantities
 684 are determined by the fit in offline reconstruction.

685 The pulse is fit to a pileup algorithm where a fit to a single pulse is compared to a fit with a
 686 double pulse. If the single pulse fit has a $\chi^2_{prob} < 0.5$, a refit with two pulses is attempted. If this
 687 produces an improved χ^2_{prob} , the double pulse fit is accepted, else the single pulse fit is accepted.
 688 The time of the pulse is corrected after the fit for several effects including a run-dependent phase
 689 shift, trigger time, and time of flight.

690 [Add plot of six samples?](#)

691 2.3.2 SVT Cluster and 3D Hit Reconstruction

692 After single strip hit reconstruction, the hits are clustered together with neighboring hits using the
693 nearest neighbor RMS Clusterer algorithm [Cite this algorithm](#). The algorithm uses the amplitudes
694 in ADC counts (where it is not necessary to convert amplitude to energy deposition) and seeds
695 hits whose amplitude are at least 4 RMS above the noise of the channel. From there, it appends
696 neighboring strips whose pulse times are within 8 ns of the seed strip and whose amplitudes are at
697 least 3 RMS above the noise of the channel. In addition, each of the strips, whether seed or neighbor
698 channel, must have a χ^2 probability for the fit in Eq. 2.3 greater than 3.20^{-6} . The position of
699 the cluster is the amplitude-weighted centroid of the hits ($\sum x_i A_i / \sum A_i$). Typically, SVT clusters
700 are composed of one or two strips hits in approximately equal proportion. Since time resolution is
701 significantly degraded for hits with low energy deposition, the time of the SVT cluster is weighted
702 by the square of the amplitude ($\sum t_i A_i^2 / \sum A_i^2$).

703 The 1D strip clusters in each axial sensor in a given layer are then paired together with the
704 corresponding stereo sensor in the same layer to form 3D hits. Only clusters within 12 ns of the
705 trigger time and with at least an amplitude of 400 ADC counts are considered. These clusters must
706 cross physically in space from the perspective of the primary (with some tolerance) and be within
707 a 16 ns coincidence of each other. A 3D hit is reconstructed at the intersection of the two strip
708 clusters. Since this intersection depends on the track angle, the 3D hit position is recalculated every
709 time the hit is used in a track fit to correct for parallax effects.

710 2.3.3 Track Reconstruction

711 The SeedTracker algorithm, which was developed for design studies with the SiD detector ([cite](#)), is
 712 performed as a simple method of track finding for HPS. Seed tracks, that is tracks that result from
 713 SeedTracker, are found using several different track finding strategies. The tracking strategies are
 714 as follows.

- 715 1. A track candidate is found using three 3D hits which forms a helical track.
- 716 2. This helix is extrapolated to a confirm layer and, if this confirm layer has a 3D hit consistent
 717 with the helix, this hit is appended to the helical trajectory. Else, the track candidate is
 718 discarded.
- 719 3. Lastly this 4-hit track is extrapolated to the remaining two layers called the extend layers. The
 720 3D hits in those layers that are consistent with the helix are appended. We require at least one
 721 of the extend layers to have a 3D hit consistent with the helix, thus requiring a minimum of
 722 five 3D hits on a track. If this extend requirement is not met, the track candidate is discarded.

723 Four tracking strategies are used because any single strategy using this method will not find
 724 tracks that miss a seed or confirm layer. The four tracking strategies used in the reconstruction are
 725 s-345 c-2 e-16, s-456 c-3 e-21, s-123 c-4 e-56, and s-123 c-5 e-46 where s, c, and e are abbreviations
 726 for seed, confirm, and extend, respectively. As an example, s-345 c-2 e-16 seeds track candidates
 727 using 3D hits on layers 3, 4, and 5. Then, this helical fit is extrapolated to layer 2, followed by layers
 728 1 and 6. The seed tracks from 345 that successfully append a hit in layer 2 and either layer 1 or 6
 729 are stored as a track candidate to be used for the remaining reconstruction.

730 In addition, there are several other requirements the track must pass. The RMS time of all
 731 the hits on the track must fall within 8 ns. The track must have a χ^2 less than 100 (including
 732 an individual hit χ^2 less than 10), a distance of closest approach $d0$ less than 15 mm, an impact
 733 parameter $z0$ of less than 15 mm, and a minimum transverse momentum of 100 MeV.

734 The SeedTracker algorithm returns a helical track fit to 3D hits, but fails to take multiple
 735 scattering into account which results in an artificially worsened momentum resolution. In order to
 736 account for multiple scattering effects, the helical track fit is refit using the General Broken Lines
 737 (GBL) algorithm [5] [11]. For HPS, the GBL algorithm treats each sensor plane in the SVT as a
 738 source of scattering and fits a track segment (defined by 5 parameters described in Sec. 2.1 that
 739 define the track state) between each sensor plane and extrapolates a track segment on the first and
 740 last SVT sensor plane. For the reconstruction of the 2016 Engineering Run dataset, the GBL track
 741 is required to have a χ^2 per degrees of freedom less than 12. The GBL fit minimizes the hit residuals
 742 and scattering angles (called kinks) for each of these track segments and provides performance
 743 equivalent to a Kalman filter. However, the GBL implementation for HPS requires 3D hits from
 744 SeedTracker before inputting the track into the GBL algorithm. This 3D hit requirement results in

⁷⁴⁵ some efficiency loss due to acceptance for particles that traverse either the axial or stereo sensor in
⁷⁴⁶ a given layer. For future track reconstruction for HPS, a Kalman filter will be used to regain this
⁷⁴⁷ loss of efficiency.

⁷⁴⁸ Add figure for tracking?

749 **2.4 Track Cluster Matching**

750 Tracks are matched to Ecal clusters by extrapolating the track state of the final SVT hit to the face
751 of the Ecal though a non-uniform magnetic field map and comparing this extrapolated position to
752 the Ecal cluster position. The track is matched with the cluster with the minimum n_σ , provided
753 that the match is less than 30σ . Analysis will impose a stricter requirement. Electron objects are
754 defined as a negatively curved GBL track that is matched to an Ecal cluster in the same detector
755 volume. Similarly, positron objects are defined as a positively curved GBL track that is matched to
756 an Ecal cluster in the same detector volume. The electron and positron objects are used as inputs
757 to the vertex fitter. The remaining Ecal clusters that do not have an associated matching track are
758 defined as photon objects.

Cut Description	Requirement
Cluster Time Difference	$ t_{e^+Cluster} - t_{e^-Cluster} < 2.5 \text{ ns}$
e^+ Track-Cluster Time Difference	$ t_{e^+Track} - t_{e^+Cluster} - 55 < 10 \text{ ns}$
e^- Track-Cluster Time Difference	$ t_{e^-Track} - t_{e^-Cluster} - 55 < 10 \text{ ns}$
Ecal clusters in opposite volumes	$y_{e^+Cluster} \times y_{e^-Cluster} < 0$
Loose track-cluster match	$\chi^2 < 15$
Beam electron cut	$p(e^-) < 2.15 \text{ GeV}$
Track Quality	$\chi^2/dof < 12$
Maximum Vertex Momentum	$V_{0p} < 2.8 \text{ GeV}$

Table 2.2: Requirements applied to V_0 particles during the reconstruction stage for data (i.e. MOUSE cuts).

Cut Description	Requirement
Cluster Time Difference	$ t_{e^+Cluster} - t_{e^-Cluster} < 5 \text{ ns}$
Track-Cluster Time Difference	$ t_{e^+Track} - t_{e^+Cluster} - 43 < 10 \text{ ns}$
Track-Cluster Time Difference	$ t_{e^-Track} - t_{e^-Cluster} - 43 < 10 \text{ ns}$
Ecal clusters in opposite volumes	$y_{e^+Cluster} \times y_{e^-Cluster} < 0$
Loose track-cluster match	$\chi^2 < 15$
Beam electron cut	$p(e^-) < 2.15 \text{ GeV}$
Track Quality	$\chi^2/dof < 6$
Maximum Vertex Momentum	$V_{0p} < 2.8 \text{ GeV}$

Table 2.3: Requirements applied to V_0 particles during the reconstruction stage for MC (i.e. MOUSE cuts).

759 2.5 Vertexing

760 Every pair of e^+ and e^- objects in an event is fitted to a Billior vertex fitter [4]. The Billior vertex
 761 fit is a fast vertex fit that finds the best-fit vertex position and track parameters based on the
 762 individual track parameters and covariance matrices of the e^+e^- pair. This provides a vertex with a
 763 reconstructed 3D position based on the distance of closest approach between the two tracks as well
 764 as a reconstructed mass and momentum that are determined based on the fitted track parameters
 765 at the fitted vertex position.

766 The Billior Vertex fit allows for additional vertex constraints. If the e^+ and e^- objects are
 767 in the same hemisphere of the detector (most likely converted bremsstrahlung), they are placed in
 768 the Unconstrained Vc Collection and not considered for this analysis. If the e^+ and e^- objects
 769 are in opposite hemispheres of the detector and they pass the MOUSE cuts (reconstruction cuts)
 770 described in Tables 2.2 and 2.3, then they are placed in the Unconstrained V0 Particle Collection and
 771 considered for the analysis. In addition, a target constraint (x , y , and z positions) and a beamspot
 772 (x and y components of the V0 momentum) are placed on the V0 particle and placed in separate
 773 collections with a one-to-one-to-one mapping between the three collections. Specifically, the target

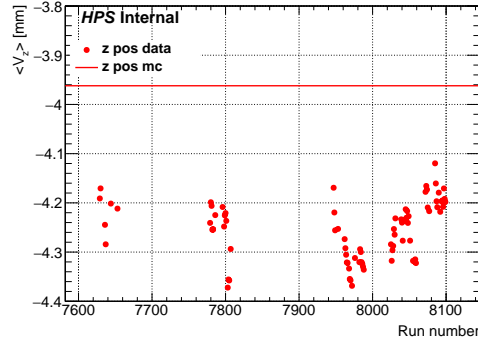


Figure 2.2: The run-dependent average position in z for unconstrained vertices fit represented by solid points and a solid line for data and MC simulation, respectively.

constraint requires the vertex to be consistent with the z position of the target and the x and y positions and sizes of the beamspot while the beamspot constraint requires the vertex momentum to point back to the beamspot at the target z position. Unconstrained vertices are used for the displaced vertex analysis while target constrained vertices are used for the resonance search.

In addition, all electron object pairs are also fit with a Billior Vertex and placed in the unconstrained Møller Candidate Vertex Collection. Møller candidates are also fit with target and beamspot constraints in separate collections and mapped in the same way. The Møller candidates are used for the studying the data/MC comparison of the mass resolution as described in Sec. ??.

The beamspot and target constrained Billior Vertex both takes use the beam position and size along with the target position in z as an input. For data, a run-by-run beam parameters were selected based on the fits of distributions. Plots for these beam parameters are shown in Fig. 2.2 and Fig. 2.3 where the data is shown as points and the MC is shown as a solid line. For MC, for simplicity and the parameters chosen to be constant and are $b_x = -0.224$ mm, $\sigma_x = 0.125$ mm, $b_y = -0.08$ mm, and $\sigma_y = 0.030$ mm. These parameters were used for both the actual simulated beam position and profile as well as inputs to the Billior Vertexer. These parameters are also used as inputs to the event selection described in Sec. ??.

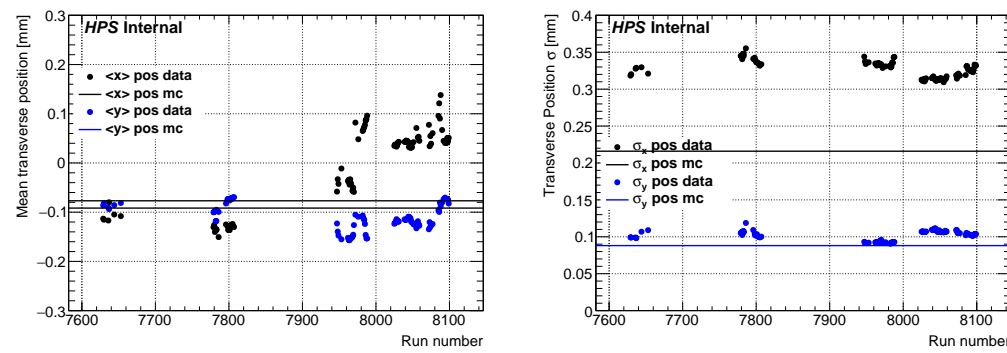


Figure 2.3: The run-dependent mean (left) and width (right) in x and y for the unconstrained vertex position in data. The MC is represented as a solid line.

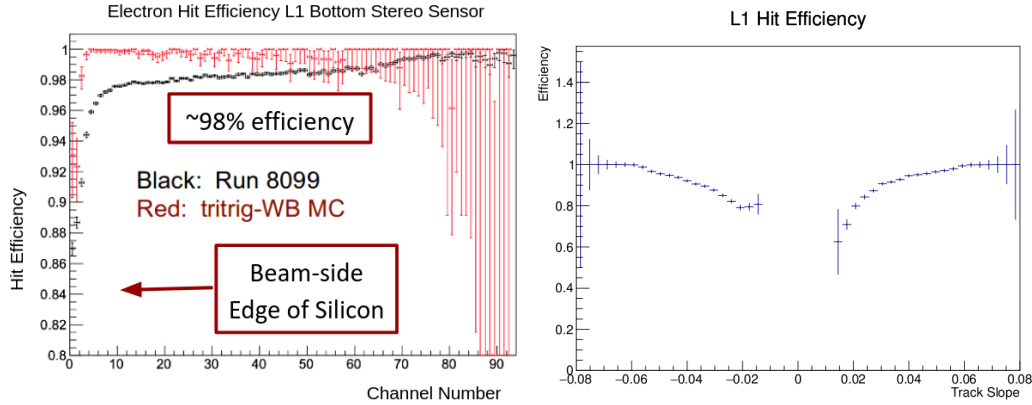


Figure 2.4: Left: The measured SVT layer 1 efficiency for electrons in layer 1 bottom stereo sensor. The MC does not have the correct hit efficiencies. Right: The layer 1 hit efficiency as a function of track slope ($\tan\lambda$) used for the hit killing algorithm described in Sec [Section.Replace these figures. Add a positron hit efficiency plot.](#)

790 2.6 Hit Efficiency

791 The HPS detector has hit efficiency effects that must be properly accounted for, particularly in the
 792 first layer of the SVT where occupancies are significantly higher than the other layers of the tracker.
 793 The main source of hit inefficiencies are wide angle bremsstrahlung conversions (WABs) in layer 1
 794 of the SVT. Positrons from converted WABs are less likely to deposit sufficient energy into a silicon
 795 strip to pass readout threshold. This could result in a track that extrapolates to the active area of a
 796 layer 1 sensor that lacks a reconstructed hit, and thus will appear as a hit inefficiency in the method
 797 described below. This can be seen in a comparison of the hit efficiencies in layer 1 for positrons
 798 and electrons in Fig. 2.4 where the difference in efficiency between electrons and positrons can be
 799 attributed to converted WABs.

800 The remaining sources of hit inefficiencies are mostly unknown and are still under exploration.
 801 One hypothesis is some of the channels are readout, but the corresponding waveforms fail the fit
 802 requirements of the hit reconstruction stage described in Sec. 2.3. There is evidence of this from the
 803 fact that hit efficiencies are dominant in layer 1 at the strips nearest to the beam plane which have
 804 the highest occupancies due to elastically-scattered beam in the target and x-ray emissions from the
 805 target.

806 Hit efficiencies are measured using a track refit to a layer of interest, and an unbiased extrapolation
 807 to that layer to see if a hit lies within a certain window of the extrapolated position. As an
 808 example, in order to measure layer 1 efficiencies, the standard track reconstruction is performed on
 809 all layers except for layer 1. The tracks that meet basic quality requirements are extrapolated to
 810 both the axial and stereo sensor planes in layer 1. For the tracks that extrapolate to the active area
 811 of the sensor of interest, if a 1D hit is not found within 5σ of the extrapolation error it is counted as

812 a hit inefficiency. The hit efficiency is defined as the ratio of the number of tracks with a hit within
813 the defined extrapolation window to the total number of tracks sampled.

814 Due to the highly non-linear nature of occupancies on the sensors, the hit efficiencies are separated
815 by channel number using the position of the extrapolated track at each sensor¹. A sample of
816 measured hit efficiency in data in comparison with MC as a function of channel number for the layer
817 1 bottom stereo sensor is shown in Fig. 2.4. In addition, there are multiple scattering effects that
818 result in a reduced measured hit efficiency on the edge of the sensors due to the fact that particle
819 trajectories that don't traverse the active sensor area reconstruct a track that extrapolates to the
820 active sensor area due to resolution effects (and thus counted as a hit inefficiency). This is most
821 visible in MC which does not contain any hit efficiencies yet has a rapidly decreasing measured
822 hit efficiency along the edge of the sensor. In principle, this can be corrected if errors on track
823 extrapolations are computed correctly.

824 Unfortunately hit efficiencies are not present in the MC, and methods of incorporating these
825 effects are under investigation. However, this effect that will affect the signal rate and distributions
826 for a variety of variables of interest. To account for hit efficiencies in both a simple and reasonable
827 way, a post-reconstruction hit killing algorithm based on track slope is applied to signal MC (and
828 some background distributions). This method is described in detail in Sec. ??.

¹The extrapolated track must be used since for an inefficiency. One cannot assign an inefficiency to a specific channel.

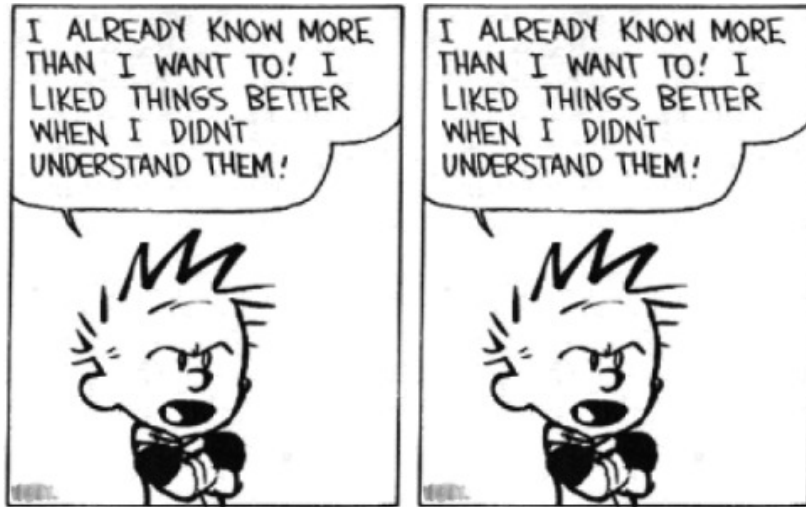


Figure 2.5: The target position is found to be -4.3 mm. I actually need to get these plots. Some placeholders are there for now.

829 2.7 Tracker Alignment

830 An initial mechanical survey is applied to the SVT as described in Sec. 1.3.2 which defines sensor
 831 positions to within a precision of $50 - 100 \mu\text{m}$. This level of imprecision will create systematic shifts
 832 in track parameters and artificially degrade tracking and vertexing resolutions, thus is insufficient
 833 to meet the HPS physics goals. In order to mitigate alignment-related effects, an offline alignment
 834 using particle trajectories to find the sensor positions and orientations as close as possible to their
 835 true values is performed.

836 Detector alignment comes in two steps - internal alignment and global alignment. The internal
 837 alignment finds the sensor positions relative to each other using the top and bottom volumes of the
 838 SVT separately with the goal of minimizing the track χ^2 . The internal alignment utilizes Millepede-
 839 II which was developed for fast alignment of large tracking detectors such as CMS [6] [7]. Each
 840 sensor can be corrected by translation along or rotation about the three coordinate axis for a total
 841 of six possible alignment corrections.

842 These corrections are not equally important. For instance, track parameters are sensitive to
 843 translations along the measurement direction in a given sensor but completely insensitive to trans-
 844 lations along the non-measurement direction (other than minor acceptance affects for track on the
 845 sensor edge). For simplicity for this alignment, only translations along the measurement direction
 846 and beam direction as well as rotations about the sensor normal were aligned **Is this true?**. The
 847 sensor position and orientations were found by iterating with different alignment configurations that
 848 float a single sensor position or orientation until the optimal alignment constant is found.

849 Global alignment involves fixing the so-called “weak modes” where sensors move in together in

such a way that the track parameters and track quality are unaffected. Since there are 5 track parameters there are 5 weak modes - translating in the horizontal ($d0$) and vertical directions ($z0$), rotating tracks horizontally (ϕ) and vertically ($\tan\lambda$), and the horizontal quadratic shear (Ω).

Elastically-scattered electrons from the target ($e^-Z \rightarrow e^-Z$) have a known momentum at the beam energy, a known origin at the beam spot on the target, and sufficiently populate the full HPS angular acceptance making them ideal to study various weak modes. First the known curvature, provides a way to study the horizontal quadratic shear. Second, the known origin provides a way to study the translational weak modes as well as the z position of the target z_{targ} . In the yz -plane the extrapolated y position of any track can be parametrized as follows:

$$y(z) = y_{beam} + \tan\lambda \times (z - z_{targ}) \quad (2.4)$$

where $\tan\lambda$ is the track slope defined in Sec. 2.1. The equation contains two unknowns - the target position in z and the beam position in y y_{beam} . This can be resolved by using both the top and bottom halves of the SVT by moving in the vertical direction until their measurements are in agreement. Similarly, the x position of the beamspot x_{beam} can be found using the same method.

Include the target position.

Møller-scattered electron pairs, that is beam electrons that scatter off of a target electron, have a known momentum equal to the momentum of the beam, including both magnitude and direction. This can be used to measure the beam angle deviation from the nominal beam axis. In addition, the two-body kinematics of Møller scattering is identical to Compton scattering and has the following relation:

$$m_e c^2 (1/E - 1/E_{beam}) = 1 - \cos \theta \quad (2.5)$$

where θ is the angle from the beam axis and E is the energy of the e^-e^- pair. As a result, all Møllers at a specific energy will scatter at the same angle from the beam axis which can be used to constrain both the rotational weak modes. Møller-scattered electrons are also useful as a “standard candle” for determining the mass scale and mass resolution as described in Sec. ??.

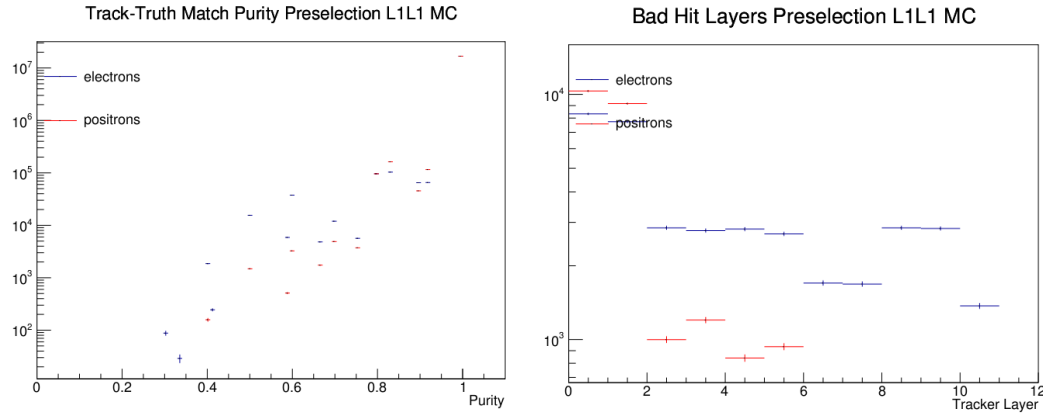


Figure 2.6: Preselection and layer 1 requirements for tritrig-wab-beam MC for e^+ and e^- tracks. Left: Purity. Right: Layers with a bad hit. **Redo these plots**

873 2.8 Track-Truth Matching

874 Due to the nature of backgrounds due to mistracking as described in Sec [Section](#), it is useful in the
 875 displaced vertex search for tracks to be matched to truth particles in the MC. This will enable a
 876 detailed study of mistracked backgrounds that can falsely reconstruct downstream of the target and
 877 appear signal-like. A simple track-truth matching algorithm is performed after reconstruction, and
 878 the algorithm is as follows:

- 879 1. In the reconstruction process, the hits on track (i.e. the tracker hits) are each mapped to a
 880 list of truth particles (called MCParticles) that contribute to the hit.
- 881 2. For each MCParticle, the number of tracker hits that the MCParticle contributes to on a given
 882 track is added.
- 883 3. The MCParticle with the highest score, that is the highest number of tracker hits, is considered
 884 to be the truth match.

885 If there is a tie in this score, the MCParticle with the inner most hits (closer to the target)
 886 is considered the to be the truth match. More precisely, a loop is performed over the tracker
 887 hits in order from first sensor to last sensor, and the MCParticle that does not contribute to
 888 a tracker hit first in this loop is no longer considered for the truth match.

889 If there is still a tie, the higher momentum MCParticle is considered to be the truth
 890 match. This last tie breaker is arbitrary and its occurrence is exceedingly rare, if ever.

891 Once an MCParticle is matched to a track, the quality of the match can be quantified by com-
 892 puting the purity of the match - which is defined as the ratio of hits the truth-matched MC particle
 893 contributes to the track to the total number of hits on track (a fraction of 10 for 5-hit tracks and a

⁸⁹⁴ fraction of 12 for 6-hit tracks). The purity of the preselection with layer one requirements of tritrig-
⁸⁹⁵ wab-beam for positrons and electrons is shown in Fig. 2.6. In this sample, about 0.002% of e^+ and
⁸⁹⁶ e^- tracks do not have a MCParticle match to track where the most likely explanation are particles
⁸⁹⁷ with truth information that is not propagated to the reconstruction level. These truth-matched
⁸⁹⁸ tracks are used to study backgrounds due to mistracking in detail.

⁸⁹⁹ 2.9 Monte Carlo Samples

Sample	Generator	Statistics
RAD	MadGraph5	~2.9M
Tritrig	MadGraph5	~8.0M
WABs	MadGraph4	~32k
A' prompt	MadGraph4	~3.8M
A' displaced	MadGraph4	~56k
Møller	EGS5	~500k
Beam	EGS5	Background

Table 2.4: Event generators and statistics for MC samples.

⁹⁰⁰ In order to be confident with the results from the analysis that it is well-understood, realistic
⁹⁰¹ Monte Carlo (MC) samples are run that specifies particular physics processes. Specifically for
⁹⁰² the background studies, we are most interested in correctly simulating trident physics processes
⁹⁰³ and converted bremsstrahlung as well as multiple and single Coulomb scattering of particles in the
⁹⁰⁴ tracker. Both prompt and displaced A' s are also simulated for signal kinematics.

⁹⁰⁵ For event generation and cross-section computation, the HPS MC chain uses several generators
⁹⁰⁶ depending on the specific physics process of interest including EGS5 [Cite EGS5](#) and MadGraph4 [2].
⁹⁰⁷ Trident processes, wide-angle bremsstrahlung (wabs), and A' 's are generated using MadGraph4. The
⁹⁰⁸ Feynman diagrams are shown in Fig. 2.7. Beam background, Møllers, and scattering in the target
⁹⁰⁹ are simulated using EGS5. All prompt processes are passed through EGS5 to properly simulate the
⁹¹⁰ scattering in the target which produces EGS5 final state particles. From EGS5 final state particles,
⁹¹¹ a package called Stdhep is used in order to persist truth information rotate and difuse the beam,
⁹¹² offset the target, and build beam bunches using a Poisson distribution for beam backgrounds.

⁹¹³ The detector response is then simulated using a GEANT4-based package [1] called Slic (Simulator
⁹¹⁴ for the Linear Collider) [9]. The detector response, specifically for the SVT and the Ecal, is converted
⁹¹⁵ into raw hits with time stamps and energy deposition information.

⁹¹⁶ Next, the raw hit information must pass through the readout simulation which emulates that
⁹¹⁷ trigger response including digitization and readout. Finally, the digitization from the readout sim-
⁹¹⁸ ulation is used as input in the physics reconstruction software in hps-java in the same way the real
⁹¹⁹ experimental data is reconstructed. This provides a way for data and simulation to be directly
⁹²⁰ compared, with MC able to be separated into different background components.

⁹²¹ The MC samples produced as shown in Table 2.4 are background samples of RAD, tritrig, WAB,
⁹²² Møller, and beam background. The A' samples come in two different types - prompt and displaced
⁹²³ from the target. Prompt A' samples are used for the resonance search and for an estimate of the
⁹²⁴ mass resolution described in Sec. ?? (mass resolution is independent of displacement). The displaced
⁹²⁵ A' 's are used to estimate the z -dependence of efficiency and geometrical acceptance. The detailed

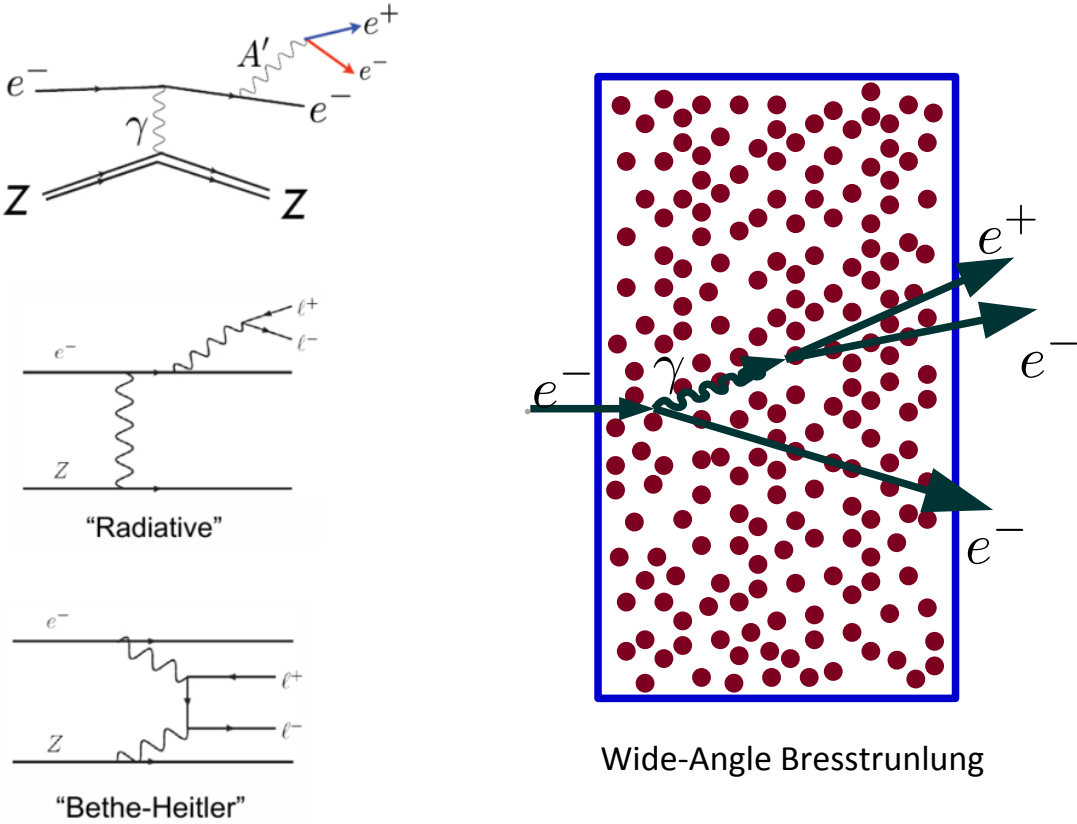


Figure 2.7: Left pictures show Feynman diagrams for A' (top), RAD (middle) and BH (bottom) events. Right picture shows WAB process.

generator level requirements for each MC sample are shown in Table 2.5.

Both prompt and displaced A' samples are generated at specific mass points over the range of interest determined by the acceptance at a specific beam energy, and with close enough spacing such that interpolation of acceptance between mass points contains minimal error. The mass points generated are between 50 MeV and 150 MeV in increments of 5 MeV as well as a high mass point at 175 MeV. The displaced A' samples must populate the decay range of interest ($\sim 0 - 150$ mm) with sufficient statistics. These samples are produced with a constant livetime at $c\tau = 10$ mm, which is a larger decay length than HPS is sensitive to for A' 's, and then reweighted at a later step to reflect actual signal shapes.

Detailed steps on the production of beam particles are as follows:

1. Beam particles are produced in EGS5.
2. Beam rotation, diffusion, and the target offset are all applied via stdhep. Beam particles are

938 sampled and beam bunches are built in stdhep.

939 3. The beam bunches are passed through Slic.

940 Detailed steps on the remaining MC - RAD, tritrig, WAB, Møllers, and A' with beam overlay -
941 are as follows:

942 1. Particles are produced in MadGraph. The exception is that Møllers are produced in EGS5.

943 2. Final state particles from MadGraph are passed through the target via EGS5. Because dis-
944 placed A' have no interaction with the target, only the recoil electron for these samples is
945 passed through the target.

946 3. Parent particles are added into each event of the EGS5 output.

947 4. Beam rotation, diffusion, and the target offset are all applied via stdhep.

948 5. The events are passed through Slic.

949 6. The output events from Slic are spaced apart by a fixed interval equal to the event window in
950 the trigger system.

Sample	Cut Description	Cut Requirement
RAD	Min energy of daughter particles	$E_{e+} > 50 \text{ MeV}$ and $E_{e-} > 50 \text{ MeV}$
RAD	Min for y -direction of e^+e^- particles	$p_{e+,y}/p_{e+} > 0.005$ and $p_{e-,y}/p_{e-} > 0.005$
RAD	Min total energy of e^+e^- pair	$E_{e+} + E_{e-} > 500 \text{ MeV}$
RAD	Min invariant mass of e^+e^- pair	$m_{e^+e^-} > 10 \text{ MeV}$
Tritrig	Min energy of e^+	$E_{e+} > 100 \text{ MeV}$
Tritrig	Min for y -direction of e^+	$p_{e+,y}/p_{e+} > 0.005$
Tritrig	Min total energy of a e^+e^- pair ²	$E_{e+} + E_{e-} > 1000 \text{ MeV}$
Tritrig	Min invariant mass of a e^+e^- pair ³	$m_{e^+e^-} > 10 \text{ MeV}$
WABs	Min photon energy	$E_\gamma > 400 \text{ MeV}$
WABs	Min for y -direction of e^+e^- particles	$p_{\gamma,y}/p_\gamma > 0.005$
Møller	Min energy of final state particles	$E > 10 \text{ MeV}$
Møller	Min for transverse direction for f.s. particles	$\sqrt{(p_x/p)^2 + (p_y/p)^2} > 0.005$
Beam	Min energy of beam particles	$E_{e-} > 0.005E_{beam}$
Beam	Min for transverse direction for f.s. particles ⁴	$\sqrt{(p_x/p)^2 + (p_y/p)^2} > 0.005$
Photon	Min for y -direction of γ	$p_{\gamma,y}/p_\gamma > 0.004$
Photon	Max for y -direction of γ ⁵	$p_{\gamma,y}/p_\gamma < 0.005$
A' 's Prompt	None	—
A' 's Displaced	None	—

Table 2.5: Basic generator level physics requirements for different physics processes.

- 951 7. The sample is mixed with the beam sample or a WAB sample if desired.
952 8. Readout and reconstruction is processed.

953 Lastly, since the displaced vertex analysis is mostly concerned with a near-zero background region
954 far beyond the target, the background shapes at the extreme tails of the reconstructed z distributions
955 must be understood. In order to do this, a sample of tridents overlaid with beam and wabs, with
956 the trident luminosity equivalent to the luminosity of the dataset, is generated. This gives some
957 indication of the high z background due to both mistracking and large scatterings in the tracker and
958 is used as a direct comparison to data in Sec. ??.

959 In addition a sample of pure tridents with about three times the luminosity in data is used to
960 further understand the tails of the z distributions due to prompt processes that undergo significant
961 multiple scattering or single Coulomb scattering and reconstruct far downstream of the target. The
962 pure trident sample is used for the high luminosity sample because overlaying a sample with beam
963 is computationally expensive.

Cut Description	Requirement
Trigger	Pair1
Track-cluster match	$\chi^2 < 10$
Cluster Time Difference	$ t_{e^+Cluster} - t_{e^-Cluster} < 1.45 \text{ ns}$
Track-Cluster Time Difference	$ t_{e^+Track} - t_{e^+Cluster} - \text{offset} < 4 \text{ ns}$
Track-Cluster Time Difference	$ t_{e^-Track} - t_{e^-Cluster} - \text{offset} < 4 \text{ ns}$
Beam electron cut	$p(e^-) < 1.75 \text{ GeV}$
Track Quality	$\chi^2/\text{dof} < 6$
Vertex Quality	$\chi^2_{unc} < 10$
Minimum e^+ Momentum	$p(e^+) > 0.4 \text{ GeV}$
Minimum e^- Momentum	$p(e^-) > 0.4 \text{ GeV}$
Maximum Vertex Momentum	$V_{0p} < 2.4 \text{ GeV}$

Table 2.6: Requirements applied to V_0 after reconstruction as an initial set to study. The time offset for data is 56 ns and the time offset for MC is 43 ns.

964 2.10 e^+e^- Preselection Cuts

965 2.11 Run Quality, Event Quality, & Data Normalization

966 Much of this info is in the analysis note.

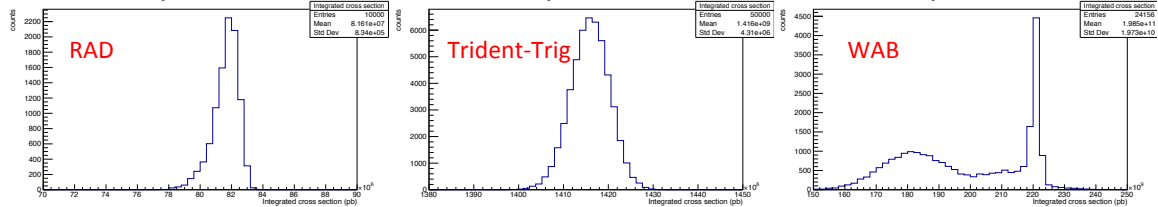


Figure 2.8: Integrated cross section for the RAD (left), Trident-Trig(middle) and WAB(right) samples, separately.

Sample	μ of ICS	σ of ICS	# of good files	# of generated events per file
RAD	81.61 μ b	0.08340 μ b	9940	10k
Trident-Trig	1.416 mb	0.004310 mb	9853	50k
WAB	0.1985 b	0.01973 b	9956	100k

Table 2.7: Normalization parameters for the RAD, Tritrig, and WAB samples

967 Normalization for MC is computed by using the mean of the integrated cross section for each
 968 sample produced as shown in Fig. 2.8 and the total number of events generated (Luminosity =
 969 Events Generated / Mean Integrated Cross-section). The results are shown in Table 2.7.

Bibliography

- [1] S. Agostinelli, J. Allison, K. Amako, J. Apostolakis, H. Araujo, P. Arce, M. Asai, D. Axen, S. Banerjee, G. Barrand, F. Behner, L. Bellagamba, J. Boudreau, L. Broglia, A. Brunengo, H. Burkhardt, S. Chauvie, J. Chuma, R. Chytracek, G. Cooperman, G. Cosmo, P. Degtyarenko, A. Dell'Acqua, G. Depaola, D. Dietrich, R. Enami, A. Feliciello, C. Ferguson, H. Fesefeldt, G. Folger, F. Foppiano, A. Forti, S. Garelli, S. Giani, R. Giannitrapani, D. Gibin, J.J. [Gmez Cadenas], I. Gonzlez, G. [Gracia Abril], G. Greeniaus, W. Greiner, V. Grichine, A. Grossheim, S. Guatelli, P. Gumplinger, R. Hamatsu, K. Hashimoto, H. Hasui, A. Heikkinen, A. Howard, V. Ivanchenko, A. Johnson, F.W. Jones, J. Kallenbach, N. Kanaya, M. Kawabata, Y. Kawabata, M. Kawaguti, S. Kelner, P. Kent, A. Kimura, T. Kodama, R. Kokoulin, M. Kossov, H. Kurashige, E. Lamanna, T. Lampn, V. Lara, V. Lefebure, F. Lei, M. Liendl, W. Lockman, F. Longo, S. Magni, M. Maire, E. Medernach, K. Minamimoto, P. [Mora de Freitas], Y. Morita, K. Murakami, M. Nagamatu, R. Nartallo, P. Nieminen, T. Nishimura, K. Ohtsubo, M. Okamura, S. O'Neale, Y. Oohata, K. Paech, J. Perl, A. Pfeiffer, M.G. Pia, F. Ranjard, A. Rybin, S. Sadilov, E. [Di Salvo], G. Santin, T. Sasaki, N. Savvas, Y. Sawada, S. Scherer, S. Sei, V. Sirotenko, D. Smith, N. Starkov, H. Stoecker, J. Sulkimo, M. Takahata, S. Tanaka, E. Tcherniaev, E. [Safai Tehrani], M. Tropeano, P. Truscott, H. Uno, L. Urban, P. Urban, M. Verderi, A. Walkden, W. Wander, H. Weber, J.P. Wellisch, T. Wenaus, D.C. Williams, D. Wright, T. Yamada, H. Yoshida, and D. Zschiesche. Geant4a simulation toolkit. *Nuclear Instruments and Methods in Physics Research Section A: Accelerators, Spectrometers, Detectors and Associated Equipment*, 506(3):250 – 303, 2003.
- [2] Johan Alwall, Pavel Demin, Simon de Visscher, Rikkert Frederix, Michel Herquet, Fabio Maltoni, Tilman Plehn, David L Rainwater, and Tim Stelzer. Madgraph/madevent v4: the new web generation. *Journal of High Energy Physics*, 2007(09):028028, Sep 2007.
- [3] N. Baltzell, H. Egiyan, M. Ehrhart, C. Field, A. Freyberger, F.-X. Girod, M. Holtrop, J. Jaros, G. Kalicy, T. Maruyama, B. McKinnon, K. Moffeit, T. Nelson, A. Odian, M. Oriunno, R. Paremuzyan, S. Stepanyan, M. Tieffenback, S. Uemura, M. Ungaro, and H. Vance. The heavy photon

- 997 search beamline and its performance. *Nuclear Instruments and Methods in Physics Research*
998 *Section A: Accelerators, Spectrometers, Detectors and Associated Equipment*, 859:69 – 75, 2017.
- 1000 [4] P. Billoir and S. Qian. Fast vertex fitting with a local parametrization of tracks. *Nuclear*
1000 *Instruments and Methods in Physics Research Section A: Accelerators, Spectrometers, Detectors*
1001 *and Associated Equipment*, 311(1):139 – 150, 1992.
- 1002 [5] V. Blobel. A new fast track-fit algorithm based on broken lines. *Nuclear Instruments and*
1003 *Methods in Physics Research Section A: Accelerators, Spectrometers, Detectors and Associated*
1004 *Equipment*, 566(1):14 – 17, 2006. TIME 2005.
- 1005 [6] V. Blobel. Software alignment for tracking detectors. *Nuclear Instruments and Methods in*
1006 *Physics Research Section A: Accelerators, Spectrometers, Detectors and Associated Equipment*,
1007 566(1):5 – 13, 2006. TIME 2005.
- 1008 [7] Volker Blobel, Claus Kleinwort, and Frank Meier. Fast alignment of a complex tracking detector
1009 using advanced track models. *Computer Physics Communications*, 182(9):1760 – 1763, 2011.
1010 Computer Physics Communications Special Edition for Conference on Computational Physics
1011 Trondheim, Norway, June 23-26, 2010.
- 1012 [8] M. J. French et al. Design and results from the APV25, a deep sub-micron CMOS front-end
1013 chip for the CMS tracker. *Nucl. Instrum. Meth.*, A466:359–365, 2001.
- 1014 [9] Norman Graf and Jeremy McCormick. Simulator for the linear collider (slic): A tool for ilc
1015 detector simulations. *AIP Conference Proceedings*, 867(1):503–512, 2006.
- 1016 [10] Norman A Graf. org.lcsim: Event reconstruction in java. *Journal of Physics: Conference Series*,
1017 331(3):032012, dec 2011.
- 1018 [11] Claus Kleinwort. General broken lines as advanced track fitting method. *Nuclear Instruments*
1019 *and Methods in Physics Research Section A: Accelerators, Spectrometers, Detectors and Asso-*
1020 *ciated Equipment*, 673:107110, May 2012.
- 1021 [12] T. Kraemer. Track Parameters in LCIO. *LC-Notes*, 2006.
- 1022 [13] T. Maruyama et al. A systematic study of polarized electron emission from strained gaas/gaasp
1023 superlattice photocathodes. *Appl. Phys. Lett.*, 85:2640, 2004.
- 1024 [14] M. Raymond et al. The CMS tracker APV25 0.25-mu-m CMOS readout chip. *Conf. Proc.*,
1025 C00091111:130–134, 2000. [130(2000)].